Towards the role of soil-well interaction on transverse kinematic response of a downhole seismometer to S-waves: a viscoelastic solution

Liming Qu[1](Aff.M.ASCE), Georges Kouroussis[2], Changwei Yang[3], Xuanming Ding[4], Yu Peng[5, *]

1 Assistant professor, Faculty of Geosciences and Environmental Engineering, Sichuan Province Engineering Technology Research Center of Ecological Mitigation of Geohazards in Tibet Plateau Transportation Corridors, Southwest Jiaotong University, Chengdu 611756, China. Email: qlming@swjtu.edu.cn.

2 Professor, Faculty of Engineering, Department of Theoretical Mechanics, Dynamics and Vibrations, Université de Mons, Belgium, E-mail: georges.kouroussis@umons.ac.be.

3 Professor, MOE Key Laboratory of High-speed Railway Engineering, College of Civil Engineering, Southwest Jiaotong University, Chengdu, 610031, China. E-mail: 1209732335@qq.com.

4 Professor, College of Civil Engineering, Key Laboratory of New Technology for Construction of Cities in Mountain Area, Chongqing University, Chongqing 400045, China. E-mail: dxmhhu@163.com.

5 Postdoctoral researcher, Department of Civil and Environmental Engineering, The Hong Kong Polytechnic University, Hung Hom, Kowloon, Hong Kong, China. Corresponding author. Email: yupeng@polyu.edu.hk.

Abstract

The seismic signal received from a seismometer installed in downhole well can be affected by soil-well interaction, leading to amplification or attenuation. This study presents a viscoelastic solution to the transverse kinematic response of the soil-well system and the signal error of a downhole seismometer subjected to S-waves. The substratum soil column beneath the downhole well is treated as a fictitious pile to facilitate a continuous analysis of the entire soil domain. The interaction between the downhole well and the surrounding soil is quantitatively formulated by the multiplication of the well displacement and a radial decay function. The validity of the proposed solution for a well is established through a comparative analysis of its specific case with two existing solutions for circular solid piles, in addition to a comparison of the well's response with numerical simulations. Signal error is defined as the relative displacement difference observed between the responses at the top and bottom of the well foundation. Parameter studies are conducted to investigate the impact of soil modulus and slender ratio of the well. The results indicate that the kinematic response factor and monitoring error are highly sensitive to incident frequency. As the frequency rises, the signal error may decrease to a consistent level but will not completely disappear. The seismometer that is installed in a shallow well and surrounded by stiff soil, tends to develop significant signal errors.

Keywords: Kinematic response; signal error; downhole seismometer; S-waves; analytical method.

Introduction

Downhole seismometers provide the potential to significantly diminish the unexpected noise emanating from the ground surface, thereby enhancing their performance in comparison to surface-deployed seismometers (Eisner et al. 2010; Horiuchi et al. 2009). In light of this merit, downhole seismometers have been used across various regions to facilitate earthquake early monitoring systems to minimize infrastructure damages (Lin et al. 2022; Lee et al. 2015; Prevedel et al. 2015). In the realm of high-speed railway networks, it is crucial that trains in the vicinity promptly decrease their speed or stop entirely in response to an earthquake event. The selection of an optimal dispatch strategy is significantly influenced by the response of transportation infrastructure to seismic excitation (Fang et al. 2023). Fig. 1 shows the train derailment and viaduct damage on Mw 7.3 earthquake in Fukushima, Japan on 16 March 2022. It was reported that an early warning system detected the compressional (P) waves and provided an opportunity to brake the train (Somerville 2022). As shown in Fig. 2, shear (S) waves travel slower than P-waves, but generally bring greater ground motion. Therefore, the post-earthquake assessment of the infrastructure damages is primarily based on the information from S-waves while the earthquake early warning for the safety of operating trains is primarily based on P-waves (Yang et al. 2023a; Zhang et al. 2021). Both the earthquake early warning and damage assessment require the acquisition of precise earthquake signals, involving the mechanism about hypocenter, path, and seismometer.

Hollender et al. (2022) identified four distinct installation methods for borehole sensors: the first method involves the use of a mechanical borehole lock; the second pertains to sand installation; the third is associated with permanently cemented sensors (refer to Theodoulidis et al. 2018); and the fourth utilizes glass beads for filling. Analogous to the third method, seismometers employed in railway engineering are often installed in downhole wells, which consist of two components: a hollow section and a foundation, both constructed from concrete material. Seismometers are positioned on the upper surface of the foundation. From a mechanical perspective, a well bears resemblance to a single cylinder comprising an upper pipe and a lower solid pile. Building on this concept, Yang et al. (2023b) formulated a theoretical model to predict the reaction of downhole wells to vertically propagating P-waves for earthquake early warning. For the case of vertically propagating S-waves, the Beam on Dynamic Winkler Foundation (BDWF) model is commonly employed for analyzing the seismic responses of piles (Fan et al. 1991; Gazetas 1984; Mylonakis 2001). Anoyatis et al. (2013) stressed the importance of boundary conditions, such as free, fixed, or hinged, at the head and tip on the kinematic responses factor (defined by the ratio of pile top displacement and free field displacement). They also identified a dimensionless frequency parameter that governs the kinematic responses of long piles. Laora and Sanctis (2013) investigated the beneficial role and filtering effects of piles in reducing seismic loading on structures. Laora and Rovithis (2015) proposed a mathematical expression to determine the active length of a pile in inhomogeneous soil. Ke and Zhang (2017) introduced a closed-form solution to analyze the kinematic bending behavior of end-bearing piles, incorporating soil shear resistance using the Pasternak model, a modified Winkler-type approach. However, Winkler-type methods may not fully capture the complex soil-structure interaction and may have limitations in accurately predicting soil responses. Treating the soil-pile system as a continuous medium, Ke et al. (2019) and Liu et al. (2014) analyzed on the transverse kinematic factor and bending moment for single piles using the modified Vlasov foundation model. Recent studies have explored the transverse seismic response of pipe by Chen et al. (2023), Zheng et al. (2022), Zhang et al. (2021), and He et al. (2020), employing the integral transform technique in continuum mechanics. However, it cannot be taken for granted that analyzing the responses and signal error of a well through the formulas for piles or pipes.

To the authors' best knowledge, there is still a lack of theoretical method for analyzing the signal error of a downhole seismometer considering soil-well interaction under S-waves. Therefore, this paper aims to develop a viscoelastic solution to examine the performance of seismometer well by extending the study by Yang et al. (2023b) from P-wave to S-wave. The modified Vlasov model (Seo and Prezzi 2007; Salgado et al. 2013; Vallabhan et al.1996) is used to implement the decoupling of soil-well interaction, thereby effectively overcoming the limitation of Winkler-type methods. The governing equations are derived using Hamilton's principle and solved through an iterative method (Basu et al. 2008; Liu et al 2014; Qu et al. 2021a; Qu et al. 2021b). To validate the present solution, the response of a specific well case, in which the inner radius approaches zero, is compared with the responses obtained from two existing solutions that are developed for piles. A numerical simulation of a well is conducted to confirm the efficiency of the present solution. The influences of the soil modulus and well dimensions on the transverse kinematic responses and signal errors are investigated. This study can offer a theoretical reference for the geometrical design of the downhole seismometer in earthquake monitoring system.

Displacement model

Problem definition

Fig. 3 depicts a downhole well to S-waves in homogeneous soil. The seismometer is installed on the upper surface of the well foundation. The downhole well is treated as a linearly elastic body with Young's modulus E_p, and density of ρ_p. The outer radius and inner radius of well are R_i and R_o, respectively. The longitudinal height H of well is constituted of the upper unfilled part L_1 and the lower filled part L_2, respectively. The surrounding soil is treated as isotropic and viscoelastic material that has Young's modulus E_s, mass density ρ_s, Poisson's ratio of υ_s and hysteretic damping ratio κ_s. The Young's modulus, shear modulus and Lame's constant for the surrounding soil can be transformed into their complex forms for dynamic analysis, i.e., $E_\mathrm{s}^* = E_\mathrm{s}\left(1+2\mathrm{i}\kappa_\mathrm{s}\right)$, $G_\mathrm{s}^* = E_\mathrm{s}^* / [2\left(1+\upsilon_\mathrm{s}\right)]$, and $\lambda_\mathrm{s}^* = E_\mathrm{s}^*\upsilon_\mathrm{s} / [(1+\upsilon_\mathrm{s})(1-2\upsilon_\mathrm{s})]$, respectively. "i" is the imaginary unit. The soil strain is assumed to remain within the small-strain range, as referenced in sources (Hardin and Drnevich 1972; Payan et al. 2016), which corresponds to the conditions observed during the majority of frequently occurring earthquakes. Due to the absence of additional structural elements atop the well, the kinematic effects and seismic forces acting on the wellhead are minimal. Furthermore, the well itself serves to attenuate seismic effects through a wave-filtering mechanism (Maria et al. 2019). As a result, the actual stress and deformation experienced by the well-soil system are relatively small except in the case of strong motion (Pilz M and Cotton, 2019). Under this condition, the well-soil system has consistent deformation, thereby preventing slippage or separation at the soil-well interface. This assumption is corroborated by previous studies (Guo and Lee 2001; Cui et al. 2023), which indicate that the contact between the well and the surrounding soil is characterized by perfect bonding. In the research conducted by Thompson et al. (2009), the soil strain is considered to be within the linear range when the maximum acceleration of the ground motion recorded by the KiK-net downhole is less than 2.0 m/s^2. This finding can be regarded as a criterion for the application of this model. The downhole well is stimulated by the harmonic S-waves propagating from the bedrock. Note also that the soil column beneath the well foundation is modelled as a fictitious soil pile, indicating its lateral deformation is constrained. The transverse ground displacement prior to the installation of a downhole seismometer is termed the free-field displacement, denoted as $u_f(z, t)$, which is independent of the variables r and θ, thus representing a one-dimensional problem. Following the establishment of a subsurface well, the well primarily deforms in the transverse direction of the S-wave, while the surrounding soil experiences deformation in three dimensions. The displacement field of the soil-well system are notably different from u_f due to wave scattering effects resulting from the contrast in stiffness between the well and the surrounding soil. In this study, it is posited that the vertical soil displacement (w_s) induced by S-waves is negligible; therefore, only the transverse (u_s) and horizontal soil displacements (v_s) are considered. The magnitude of the wave-scattering effect is directly proportional to the disparity between the actual displacement and the free-field displacement. Consequently, the relative displacement between the seismic well and the free-field soil reaches its maximum at the the outer edge of the well. In contrast, at soil positions sufficiently distant from the well, the wave-scattering effect is minimal and can be disregarded. An attenuation function $\phi(r)$ is introduced to quantitatively describe the degree of wave scattering effect at various radial positions. Accordingly, the displacement field of the soil domain can be expressed in the following forms:

$$\begin{cases} u_{\mathrm{si}}(r,\theta,z,t) = \left\{u_{\mathrm{f}}(z,t) - \left[u_{\mathrm{f}}(z,t) - u_{\mathrm{pi}}(z,t)\right]\phi(r)\right\}\cos\theta \\ v_{\mathrm{si}}(r,\theta,z,t) = -\left\{u_{\mathrm{f}}(z,t) - \left[u_{\mathrm{f}}(z,t) - u_{\mathrm{pi}}(z,t)\right]\phi(r)\right\}\sin\theta \\ w_{\mathrm{si}}(r,\theta,z,t) = 0 \end{cases} \tag{1}$$

where u_{pi}, i=1, 2, 3 represents the transverse displacements of the hollow section, well foundation and the fictitious soil pile, respectively. u_{si} represents the transverse displacements of the soils surrounding the hollow section, well foundation and the fictitious soil pile. Considering the perfect bond condition as soil-well interface, u_s should equals u_p when r=R_o. Naturally, the influences of well should be trivial when r approaches infinity. Therefore, decay function $\phi(r)$ has following boundary conditions:

$$\begin{cases} \phi(r)\big|_{r=R_o} = 1 \\ \phi(r)\big|_{r=\infty} = 0 \end{cases} \tag{2}$$

Free-field displacement

Under the harmonic excitation, the ground motion is also harmonic with $e^{i\omega t}$. For simplicity, $e^{i\omega t}$ will be omitted in the following sections unless it is necessary. Let u_g denotes the displacement of the bedrock. $U_f(z)$ denote the relative displacement of free field with respect to the bedrock. The free-field displacement in soil under vertically incident S-waves can be expressed as:

$$u_f(z) = U_f(z) + u_g \tag{3}$$

Employing Hamilton's principle and collecting the coefficients of $\delta U_f(z)$ can yield the following general solution of $U_f(z)$:

$$U_f(z) = A\cos(\lambda_f z) + B\sin(\lambda_f z) - u_g \tag{4}$$

where $\lambda_f^2 = \rho_s \omega^2 / G_s^*$; A and B are unknown coefficients which can be determined by following boundary conditions:

$$\frac{dU_f(z)}{dz} = 0 \ (z = 0) \tag{5a}$$

$$U_f(L) = 0 \tag{5b}$$

Here A and B are directly given by the following:

$$A = \frac{u_g}{\cos(\lambda_f L)} \tag{6a}$$

$$B = 0 \tag{6b}$$

The solution of free-field displacement $u_f(z)$ can be expressed as:

$$u_f(z) = \frac{u_g}{\cos(\lambda_f L)}\cos(\lambda_f z) \tag{7}$$

Energy formations and Hamilton's principle in a well-soil system

The relationship between stress and strain in a viscoelastic soil medium is written as:

$$\begin{bmatrix}\sigma_{zz}\\ \sigma_{rr}\\ \sigma_{\theta\theta}\\ \tau_{rz}\\ \tau_{z\theta}\\ \tau_{r\theta}\end{bmatrix}=\begin{bmatrix}\lambda_s^*+2G_s^* & \lambda_s^* & \lambda_s^* & 0 & 0 & 0\\ \lambda_s^* & \lambda_s^*+2G_s^* & \lambda_s^* & 0 & 0 & 0\\ \lambda_s^* & \lambda_s^* & \lambda_s^*+2G_s^* & 0 & 0 & 0\\ 0 & 0 & 0 & G_s^* & 0 & 0\\ 0 & 0 & 0 & 0 & G_s^* & 0\\ 0 & 0 & 0 & 0 & 0 & G_s^*\end{bmatrix}\begin{bmatrix}\varepsilon_{zz}\\ \varepsilon_{rr}\\ \varepsilon_{\theta\theta}\\ \gamma_{rz}\\ \gamma_{z\theta}\\ \gamma_{r\theta}\end{bmatrix} \tag{8}$$

According to the assumptions in the displacement model shown in Fig. 3, the relationship between displacement and strain components for soil is given by:

$$\begin{bmatrix}\varepsilon_{zz}\\ \varepsilon_{rr}\\ \varepsilon_{\theta\theta}\\ \gamma_{rz}\\ \gamma_{z\theta}\\ \gamma_{r\theta}\end{bmatrix}=\begin{bmatrix}-\frac{\partial w_{si}}{\partial z}\\ -\frac{\partial u_{si}}{\partial r}\\ -\frac{\partial u_{si}}{r}-\frac{1}{r}\frac{\partial v_{si}}{\partial \theta}\\ -\frac{\partial w_{si}}{\partial r}-\frac{\partial u_{si}}{\partial z}\\ -\frac{1}{r}\frac{\partial w_{si}}{\partial \theta}-\frac{\partial v_{si}}{\partial z}\\ -\frac{1}{r}\frac{\partial u_{si}}{\partial \theta}-\frac{\partial v_{si}}{\partial r}+\frac{v_{si}}{r}\end{bmatrix}=\begin{bmatrix}0\\ -\frac{\partial u_{si}}{\partial r}\\ 0\\ -\frac{\partial u_{si}}{\partial z}\\ -\frac{\partial v_{si}}{\partial z}\\ -\frac{\partial v_{si}}{\partial r}\end{bmatrix} \tag{9}$$

Substituting Eq. (9) into Eq. (8), the strain energy Π_{soil} in soil can be expressed as:

$$\begin{aligned}\Pi_{soil}&=\frac{1}{2}\int_0^{2\pi}\int_{R_0}^{\infty}\int_0^{L}(\sigma_{rr}\varepsilon_{rr}+\tau_{rz}\gamma_{rz}+\tau_{z\theta}\gamma_{z\theta}+\tau_{r\theta}\gamma_{r\theta})rdzdrd\theta\\ &=\frac{1}{2}\int_0^{2\pi}\int_{R_0}^{\infty}\int_0^{L}\left[\left(\lambda_s^*+2G_s^*\right)\left(\frac{\partial u_{si}}{\partial r}\right)^2+G_s^*\left(\frac{\partial u_{si}}{\partial z}\right)^2+G_s^*\left(\frac{\partial v_{si}}{\partial z}\right)^2+G_s^*\left(\frac{\partial v_{si}}{\partial r}\right)^2\right]rdzdrd\theta\end{aligned} \tag{10}$$

The kinetic energy of the soil is written as follows:

$$T_{soil}=\frac{1}{2}\int_0^{2\pi}\int_R^{\infty}\int_0^{L}\rho_s\left(\frac{\partial u_{si}}{\partial t}+\frac{\partial v_{si}}{\partial t}\right)^2 rdzdrd\theta \tag{11}$$

Similarly, the strain energy Π_{pile} and the kinetic energy T_{pile} in the pile and soil pile can be expressed as:

$$\Pi_{pile}=\frac{1}{2}E_pI_{p1}\int_0^{L_1}\left(\frac{d^2u_{p1}}{dz^2}\right)^2dz+\frac{1}{2}E_pI_{p2}\int_{L_1}^{L_1+L_2}\left(\frac{d^2u_{p2}}{dz^2}\right)^2dz+\frac{1}{2}\int_H^{L}G_s^*A_{p3}\left(\frac{du_{p3}}{dz}\right)^2dz \tag{12}$$

$$T_{\text{pile}} = \frac{1}{2}\int_0^{L_1} \rho_{\text{p}} A_{\text{p1}} \left(\frac{du_{\text{p1}}}{dt}\right)^2 dz + \frac{1}{2}\int_{L_1}^{L_1+L_2} \rho_{\text{p}} A_{\text{p2}} \left(\frac{du_{\text{p1}}}{dt}\right)^2 dz + \frac{1}{2}\int_H^L \rho_{\text{p}} A_{\text{p3}} \left(\frac{du_{\text{p3}}}{dt}\right)^2 dz \quad (13)$$

where E^*_{p1} and I_{p1} are the complex elastic modulus and the moment of inertia of the hollow section, while E^*_{p2} and I_{p2} denote the corresponding properties for the well foundation. A_{p1}, A_{p2} and A_{p3} are the cross-section areas of the hollow section, well foundation and the fictitious soil column, respectively. Let function $\Re$ represents for the total energy of the well-soil system during the period from t_1 to t_2 . Based on the Hamilton variational principle, the prerequisite of equilibrium status for a soil-well system is that the variation $\delta\Re$ has its minimal value, which yields:

$$\delta\Re = \int_{t_1}^{t_2} (T_{\text{pile}} + T_{\text{soil}} - \Pi_{\text{pile}} - \Pi_{\text{soil}}) dt = 0 \quad (14)$$

Governing equations and solving process

Displacement of the soil column u_{p3}

Substituting $u_{\text{p3}}(z,t) = u_{\text{p3}}(z)e^{i\omega t}$, considering Hamilton's principle and collecting the coefficients of δu_{p3}, the governing equation of u_{p3} for the fictitious soil pile can be obtained as:

$$\left[\left(\lambda_{\text{s}}^* + G_{\text{s}}^*\right)\pi + \pi G_{\text{s}}^*\right] \int_H^L \int_{R_{\text{o}}}^{\infty} \left(\frac{\partial \phi}{\partial r}\right)^2 \left[u_{\text{p3}}(z) - u_{\text{f}}(z)\right] \delta u_{\text{p3}} r dr dz - 2\pi G_{\text{s}}^* \left(\int_{R_{\text{o}}}^{\infty} \phi^2 r dr\right) \int_H^L \frac{\partial^2 u_{\text{p3}}(z)}{\partial z^2} \delta u_{\text{p3}}(z) dz$$
$$-G_{\text{s}}^* A_{\text{p3}} \int_H^L \frac{d^2 u_{\text{p3}}}{dz^2} dz \delta u_{\text{p3}} dz - 2\pi \rho_{\text{s}} \omega^2 \left(\int_R^{\infty} \phi^2 r dr\right) u_{\text{p3}}(z) \delta \int_R^{\infty} \int_H^L u_{\text{p3}}(z) dz dr - \rho_{\text{p}} A_{\text{p3}} \omega^2 \int_H^L u_{\text{p3}} \delta u_{\text{p3}} dz = 0$$
(15)

Simplifying Eq. (15) produces the following:

$$\frac{d^2 u_{\text{p3}}}{dz^2} - k^2 u_{\text{p3}}(z) = -\xi u_{\text{f}}(z) \quad (16)$$

where the coefficients k, α, β, ϑ and ξ can be calculated as follows:

$$k=\sqrt{\frac{\alpha-\left(\beta+A_{\mathrm{p3}}\rho_{\mathrm{p}}\right)\omega^2}{G_{\mathrm{s}}^*A_{\mathrm{p}}+\vartheta}} \tag{17a}$$

$$\alpha=\left(\lambda_{\mathrm{s}}^*+3G_{\mathrm{s}}^*\right)\pi\int_{R_{\mathrm{o}}}^{\infty}\left[\frac{\partial\phi(r)}{\partial r}\right]^2 rdr \tag{17b}$$

$$\beta=2\pi\rho_{\mathrm{s}}\int_{R_{\mathrm{o}}}^{\infty}\phi^2 rdr \tag{17c}$$

$$\vartheta=2\pi G_{\mathrm{s}}^*\left(\int_{R_{\mathrm{o}}}^{\infty}\phi^2 rdr\right) \tag{17d}$$

$$\xi=\frac{\alpha}{G_{\mathrm{s}}^*A_{\mathrm{p3}}+\vartheta} \tag{17e}$$

The general solution of Eq. (16) can be written as:

$$u_{\mathrm{p3}}=De^{kz}+Fe^{-kz}+\varsigma u_{\mathrm{f}}(z) \tag{18}$$

where the coefficient ς can be given by:

$$\varsigma=\xi/\left(\lambda_{\mathrm{f3}}^2+k^2\right) \tag{19}$$

Substituting Eq. (17a) and Eq. (17e) into (19) produces $\varsigma=1$. Unknown coefficients *D* and *F* in Eq. (18) can be determined from the following two boundary conditions:

$$u_{\mathrm{p3}}=u_{\mathrm{p2}}, z{=}H \tag{20a}$$

$$u_{\mathrm{p3}}=u_{\mathrm{g}}, z{=}L \tag{20b}$$

Finally, the displacement of soil column can be expressed as:

$$u_{\mathrm{p3}}=\mathrm{csch}(kH-kL)\left[u_{\mathrm{p2}}(H)-u_{\mathrm{f}}(H)\right]\sinh(kz-kL)+u_{\mathrm{f}}(z) \tag{21}$$

Displacement u_{p} of the well

Considering Hamilton's principle and collecting the coefficients of δu_{pi} (i=1, 2), the governing equation of u_{pi} for the well displacement can be obtained as:

$$
\begin{aligned}
&E_{\mathrm{p}} I_{\mathrm{pi}} \int_{L_{\mathrm{i-1}}}^{L_{\mathrm{i}}} \frac{d^4\left(u_{\mathrm{pi}}\right)}{dz^4} dz - 2\pi G_{\mathrm{s}}^* \int_R^{\infty} \phi^2 r dr \int_{L_{\mathrm{i-1}}}^{L_{\mathrm{i}}} \frac{\partial^2 u_{\mathrm{pi}}(z)}{\partial z^2} dz \\
&+ \int_{L_{\mathrm{i-1}}}^{L_{\mathrm{i}}} \left\{ \left[\left(\lambda_s^* + G_s^* \right) \pi + \pi G_{\mathrm{s}}^* \right] \int_R^{\infty} \left(\frac{\partial \phi}{\partial r} \right)^2 r dr - 2\pi \rho_{\mathrm{s}} \omega^2 \left(\int_R^{\infty} \phi^2 r dr \right) - \rho_{\mathrm{p}} A_{\mathrm{p}} \omega^2 \right\} u_{\mathrm{pi}}(z) dz \qquad (22) \\
&- \left[\left(\lambda_{\mathrm{s}}^* + G_{\mathrm{s}}^* \right) \pi + \pi G_{\mathrm{s}}^* \right] \int_R^{\infty} \left(\frac{\partial \phi}{\partial r} \right)^2 r dr \int_{L_{\mathrm{i-1}}}^{L_{\mathrm{i}}} u_{\mathrm{f}}(z) dz = 0, \quad i = 1,\ 2
\end{aligned}
$$

Simplifying Eq. (22) yields the following:

$$
\frac{d^4\left(u_{\mathrm{pi}}\right)}{dz^4} - \frac{\vartheta}{E_{\mathrm{p}} I_{\mathrm{pi}}} \frac{d^2 u_{\mathrm{pi}}(z)}{dz^2} + \psi_{\mathrm{i}}{}^4 u_{\mathrm{pi}}(z,t) = \frac{\alpha}{E_{\mathrm{p}} I_{\mathrm{pi}}} u_{\mathrm{f}}(z,t) \qquad (23)
$$

where ϑ and α can refer to Eq. 17. The coefficient ψ_{i} is given by:

$$
\psi_{\mathrm{i}} = \left[\frac{\alpha - \left(\beta + \rho_{\mathrm{pi}} A_{\mathrm{pi}} \right) \omega^2}{E_{\mathrm{p}} I_{\mathrm{pi}}} \right]^{\frac{1}{4}} \qquad (24)
$$

The general solution of Eq. (23) can be expressed as:

$$
u_{\mathrm{pi}}(z) = c_{1\mathrm{i}} f_{1\mathrm{i}}(z) + c_{2i} f_{2\mathrm{i}}(z) + c_{3\mathrm{i}} f_{3\mathrm{i}}(z) + c_{4\mathrm{i}} f_{4\mathrm{i}}(z) + \chi_{\mathrm{pi}} u_{\mathrm{f}}(z) \qquad (25)
$$

where f_{ji} and c_{ji} are solution functions and their corresponding unknown coefficients, respectively. The coefficient χ_{pi} is given by:

$$
\chi_{\mathrm{pi}} = \frac{\alpha}{E_{\mathrm{p}} I_{\mathrm{pi}}} \Big/ \left(\lambda_{\mathrm{f}}^4 + \frac{\vartheta}{E_{\mathrm{p}} I_{\mathrm{pi}}} \lambda_{\mathrm{f}}^2 + \psi_{\mathrm{i}}{}^4 \right) \qquad (26)
$$

When $\left(\vartheta / E_{\mathrm{p}} I_{\mathrm{pi}} \right)^2 \geq 4\psi_{\mathrm{i}}^4$, the vector function $\overrightarrow{f_{\mathrm{ji}}}$ can be expressed as the following:

$$
\overrightarrow{f_{\mathrm{ji}}} = \left[f_{1\mathrm{i}}(z) \quad f_{2\mathrm{i}}(z) \quad f_{3\mathrm{i}}(z) \quad f_{4\mathrm{i}}(z) \right] = \left[\sinh(\lambda_{\mathrm{i}}^1 z) \quad \cosh(\lambda_{\mathrm{i}}^1 z) \quad \sinh(\lambda_{\mathrm{i}}^2 z) \quad \cosh(\lambda_{\mathrm{i}}^2 z) \right] \qquad (27)
$$

where it has:

$$
\lambda_{\mathrm{i}}^1 = \frac{\vartheta}{2 E_{\mathrm{pi}}^* I_{\mathrm{pi}}} + \sqrt{\frac{1}{4} \left(\frac{\vartheta}{E_{\mathrm{pi}}^* I_{\mathrm{pi}}} \right)^2 - \psi_{\mathrm{i}}^4} \qquad (28a)
$$

$$\lambda_{\mathrm{i}}^{2}=\frac{\vartheta}{2E_{\mathrm{pi}}^{*}I_{\mathrm{pi}}}-\sqrt{\frac{1}{4}\left(\frac{\vartheta}{E_{\mathrm{pi}}^{*}I_{\mathrm{pi}}}\right)^{2}-\psi_{\mathrm{i}}^{4}} \tag{28b}$$

when $\left(\vartheta / E_{\mathrm{pi}}^{*}I_{\mathrm{pi}}\right)^{2}<4\psi_{\mathrm{i}}^{4}$, the vector function $\overrightarrow{f_{\mathrm{ji}}}$ can be expressed as follows:

$$\begin{aligned}\overrightarrow{f_{\mathrm{ji}}}&=\left[f_{1\mathrm{i}}(z)\quad f_{2\mathrm{i}}(z)\quad f_{3\mathrm{i}}(z)\quad f_{4\mathrm{i}}(z)\right]\\&=\left[\sinh(\lambda_{\mathrm{i}}^{3}z)\cos(\lambda_{\mathrm{i}}^{4}z)\quad \cosh(\lambda_{\mathrm{i}}^{3}z)\sin(\lambda_{\mathrm{i}}^{4}z)\quad \sinh(\lambda_{\mathrm{i}}^{3}z)\sin(\lambda_{\mathrm{i}}^{4}z)\quad \cosh(\lambda_{\mathrm{i}}^{3}z)\cos(\lambda_{\mathrm{i}}^{4}z)\right]\end{aligned} \tag{29}$$

where it has:

$$\lambda_{\mathrm{i}}^{3}=\sqrt{\frac{1}{4}\left(\frac{\vartheta}{E_{\mathrm{p}}I_{\mathrm{pi}}}\right)+\frac{1}{2}\psi_{i}^{2}} \tag{30a}$$

$$\lambda_{\mathrm{i}}^{4}=\sqrt{-\frac{1}{4}\left(\frac{\vartheta}{E_{\mathrm{p}}I_{\mathrm{pi}}}\right)+\frac{1}{2}\psi_{\mathrm{i}}^{2}} \tag{30b}$$

Boundary conditions of Eq. (25) can be written according to the moment and shear stress characteristics of seismic well as follows:

$$\frac{d^{2}u_{\mathrm{p1}}}{dz^{2}}=0, z=0 \tag{31a}$$

$$E_{\mathrm{p}}I_{\mathrm{p1}}\frac{d^{3}u_{\mathrm{p1}}}{dz^{3}}-\vartheta\frac{du_{\mathrm{p1}}}{dz}=0,\ (z=0) \tag{31b}$$

$$\frac{d^{2}u_{\mathrm{p2}}}{dz^{2}}=0,\ (z=H) \tag{31c}$$

$$E_{\mathrm{p}}I_{\mathrm{p2}}\frac{d^{3}u_{\mathrm{p2}}}{dz^{3}}-\vartheta\frac{du_{\mathrm{p2}}}{dz}+(\vartheta+G_{\mathrm{s}}^{*}A_{\mathrm{p2}})\frac{du_{\mathrm{p3}}}{dz}=0,\ (z=H) \tag{31d}$$

$$u_{\mathrm{p1}}=u_{\mathrm{p2}},\ (z=L_{1}) \tag{31e}$$

$$\frac{du_{\mathrm{p1}}}{dz}=\frac{du_{\mathrm{p2}}}{dz},\ (z=L_{1}) \tag{31f}$$

$$\frac{d^{2}u_{\mathrm{p1}}}{dz^{2}}=\frac{d^{2}u_{\mathrm{p2}}}{dz^{2}},\ (z=L_{1}) \tag{31g}$$

$$E_{\mathrm{p}}I_{\mathrm{p1}}\frac{d^{3}u_{\mathrm{p1}}}{dz^{3}}-\vartheta\frac{du_{\mathrm{p1}}}{dz}=E_{\mathrm{p}}I_{\mathrm{p2}}\frac{d^{3}u_{\mathrm{p2}}}{dz^{3}}-\vartheta\frac{du_{\mathrm{p2}}}{dz},\ (z=L_{1}) \tag{31h}$$

Let the vectors $\left[C_1\right]=\left[c_{11} \quad c_{12} \quad c_{13} \quad c_{14}\right]^T, \left[C_2\right]=\left[c_{21} \quad c_{22} \quad c_{23} \quad c_{24}\right]^T$, the solution of c_{ij} can be expressed as following:

$$\begin{bmatrix} C_1 \\ C_2 \end{bmatrix} = \begin{bmatrix} M_{11} & M_{12} \\ M_{21} & M_{22} \end{bmatrix}^{-1} \begin{bmatrix} P_1 \\ P_2 \end{bmatrix} \tag{32}$$

where the 4×4 block matrices M_{11}, M_{12}, M_{21}, and M_{22} can be given by:

$$M_{11} = \left[\vec{f}\,''_{\mathrm{j1}}(0) \quad \vec{f}\,'''_{\mathrm{j1}}(0) - \frac{\vartheta}{E_{\mathrm{p}} I_{\mathrm{p1}}} \vec{f}\,'_{\mathrm{j1}}(0) \quad \mathbf{0} \quad \mathbf{0} \right]^{\mathrm{T}} \tag{33}$$

$$M_{12} = \left[\mathbf{0} \quad \mathbf{0} \quad \vec{f}\,''_{\mathrm{i2}}(H) \quad \vec{f}\,'''_{\mathrm{i2}}(H) - \frac{\vartheta}{E_{\mathrm{p}} I_{\mathrm{p2}}} \vec{f}\,'_{\mathrm{i2}}(H) + \frac{(\vartheta + G_{\mathrm{s}}^* A_{\mathrm{p2}})}{E_{\mathrm{p}} I_{\mathrm{p2}}} k\coth(kH - kL) \vec{f}_{\mathrm{i2}}(H) \right]^T \tag{34}$$

$$M_{21} = \left[\vec{f}_{\mathrm{i1}}(L_1) \quad \vec{f}\,'_{\mathrm{i1}}(L_1) \quad \vec{f}\,''_{\mathrm{i1}}(L_1) \quad E_{\mathrm{p1}}^* I_{\mathrm{p1}} \vec{f}\,'''_{\mathrm{i1}}(L_1) - \vartheta \vec{f}\,'_{\mathrm{i1}}(L_1) \right]^{\mathrm{T}} \tag{35}$$

$$M_{22} = \left[-\vec{f}_{\mathrm{i2}}(L_1) \quad -\vec{f}\,'_{\mathrm{i2}}(L_1) \quad -\vec{f}\,''_{\mathrm{i2}}(L_1) \quad -E_{\mathrm{p2}}^* I_{\mathrm{p2}} \vec{f}\,'''_{\mathrm{i2}}(L_1) + \vartheta \vec{f}\,'_{\mathrm{i2}}(L_1) \right]^{\mathrm{T}} \tag{36}$$

$$\left[P_1\right] = \begin{bmatrix} -\chi_{\mathrm{p1}} u''_{\mathrm{f}}(0) \\ -\chi_{\mathrm{p1}} u'''_{\mathrm{f}}(0) + \chi_{\mathrm{p1}} \dfrac{\vartheta}{E_{\mathrm{p}} I_{\mathrm{p1}}} u'_{\mathrm{f}}(0) \\ -\chi_{\mathrm{p2}} u''_{\mathrm{f}}(H) \\ -\chi_{\mathrm{p2}} u'''_{\mathrm{f}}(H) + \dfrac{\vartheta}{E_{\mathrm{p}} I_{\mathrm{p2}}} \chi_{\mathrm{p2}} u'_{\mathrm{f}}(H) - \dfrac{(\vartheta + G_{\mathrm{s}}^* A_{\mathrm{p2}})}{E_{\mathrm{p2}} I_{\mathrm{p2}}} \left[\left(\chi_{\mathrm{p2}} - 1 \right) u_{\mathrm{f}}(H) k\coth(kH - kL) + u'_{\mathrm{f}}(H) \right] \end{bmatrix} \tag{37}$$

$$\left[P_2\right] = \begin{bmatrix} \left(\chi_{\mathrm{p2}} - \chi_{\mathrm{p1}} \right) u_{\mathrm{f}}(L_1) \\ \left(\chi_{\mathrm{p2}} - \chi_{\mathrm{p1}} \right) u'_{\mathrm{f}}(L_1) \\ \left(\chi_{\mathrm{p2}} - \chi_{\mathrm{p1}} \right) u''_{\mathrm{f}}(L_1) \\ \left(E_{\mathrm{p2}}^* I_{\mathrm{p2}} \chi_{\mathrm{p2}} - E_{\mathrm{p1}}^* I_{\mathrm{p1}} \right) u'''_{\mathrm{f}}(L_1) - \vartheta \left(\chi_{\mathrm{p2}} - \chi_{\mathrm{p1}} \right) u'_{\mathrm{f}}(L_1) \end{bmatrix} \tag{38}$$

Attenuation function $\phi(r)$

Collecting the coefficients of $\delta\phi$ produces the governing equation of ϕ as following:

$$\frac{d\phi^2}{dr^2}+\frac{1}{r}\frac{d\phi}{dr}-q^2\phi=0 \tag{39}$$

where the coefficient q can be given by:

$$q=\sqrt{\frac{2G_s^*}{\left(\lambda_s^*+3G_s^*\right)}\frac{\sum_{i=1}^{3}\int_{L_{i-1}}^{L_i}\left[\frac{\partial}{\partial z}u_f(z)-\frac{\partial}{\partial z}u_{pi}(z)\right]^2 dz}{\sum_{i=1}^{i=3}\int_{L_{i-1}}^{L_i}\left[u_{pi}(z)\text{-}u_f(z)\right]^2 dz}+\frac{2\rho_s\omega^2}{\lambda_s^*+3G_s^*}} \tag{40}$$

Combining with the boundary condition in Eq. (2), the solution to Eq. (39) is given by:

$$\phi(r)=K_0(qr)/K_0(qR_o) \tag{41}$$

where $K_0(\bullet)$ is the second modified Bessel function of order zero.

Solution technique

According to the studies by Mylonakis (2001) and Liu et al (2014), in order to removing the high sensitivity to Poisson's ratio of in stress-strain relationship, soil modulus E_s^* and the lame constant λ_s^* is replaced with $[1-2\upsilon_s^2/\left(1-\upsilon_s\right)]E_s^*$ and $2\upsilon_s G_s^*$, respectively. Furthermore, the aforementioned unknown parameter ϑ α, β, ψ, λ, χ, are involved with each other, which requires an iterative method for final values. Here the fixed-point iteration is employed, which follows the flow chart shown in Fig. 4. Similar method has been successfully used in the domain of pile-soil interaction by Seo and Prezzi (2007) and Salgado et al. (2013).

In order to confirm the robustness of convergence with respect to initial value q_0, three cases with various frequencies: f=0.0001Hz, 5.0Hz and 10.0Hz are calculated using this present method. The permissible error for the absolute value of q, determined by the difference in results from adjacent iterations, is set to 0.001. Fig. 5 illustrates the variation of q with different initial values q_0: 1.0, 1.0+0.1i, and 10.0. The findings indicate that all iteration processes for q converge within 10 cycles for both the real and imaginary parts, suggesting that the convergence is not significantly influenced by the initial value.

After the iterations have converged, the kinematic response factor at the head of seismometer well can be written in the form of transverse displacement ratio as follows (Anoyatis et al. 2013):

$$I_{\mathrm{u}} = \frac{u_{\mathrm{p1}}(0)}{u_{\mathrm{f}}(0)} \tag{42}$$

The signal error is defined as the following Yang et al. (2023a):

$$E_{\mathrm{r}} = \frac{u_{\mathrm{foundation}}(L_1) - u_{\mathrm{foundation}}(H)}{u_{\mathrm{foundation}}(H)} \times 100\% \tag{43}$$

where $u_{\mathrm{foundation}}(L_1)$ and $u_{\mathrm{foundation}}(H)$ are the transverse displacement at the top and bottom of the well foundation, respectively. This study examines the role of soil-well interaction on the transverse kinematic response from a theoretical perspective. It is important to note that potential sources of noise or non-linear effects, such as sensor tilting, are not accounted for in Eq. (43).

Comparisons and verification

Liu et al. (2014) and Anoyatis et al. (2013) have presented solutions in frequency domain for the kinematic response of solid piles subjected to S-waves in homogenous soil. The downhole seismometer well has a similar structure with a solid pile when the well's inner radius R_{i} =0. Fig. 6 illustrates a comparison between the kinematic response factor I_{u} from this current study and the previously published solutions. The frequency has been normalized into a nondimensional form $a_0=\omega d/V_{\mathrm{s}}$ to account for the influences of well diameter (d=2R_{o}) and soil wavelength on response characteristics. The results depicted in Fig. 5 indicate that all three methods show similar variations in I_{u} versus a_0. The kinematic response factor I_{u} equals 1 when a_0=0, which can be understood in light of the specific solutions provided: $u_{\mathrm{p1}}(z) = u_{\mathrm{f}}(z), u_{\mathrm{p2}}(z) = u_{\mathrm{f}}(z), u_{\mathrm{p3}}(z) = u_{\mathrm{f}}(z), u_{\mathrm{f}}(z) = u_{\mathrm{g}}$ satisfy all the governing equations and boundary conditions in the last section. As frequency increases, the value of I_{u} increases until it reaches a maximum point after which it begins to decline within the specified frequency range of a_0<0.5, which confirms the validation of the present method. It is also observed that in Fig. 5 that this present solution overall agrees well with Liu et al. (2014). Slight deviation between the results of in Anoyatis et al. (2013) and this present solution occurs when a_0>0.3 for $E_{\mathrm{p}}/E_{\mathrm{s}}$=1000. The reason for this is that the Winkler model used in Anoyatis et al. (2013) represents soil reaction with discrete springs and thus neglects the effects of surrounding soil continuity on the shear resistance.

To the authors' best knowledge, reference results in the case of non-zero R_i are very few. In order to test the model's validity for a seismic well with finite hollow sections, numerical simulations were performed using the Finite Difference code FLAC3D. Calculation of the displacement of the well-soil system was achieved using a linear elastic soil model a density of ρ_s=1800kg/m^3, Young's modulus of E_s=200MPa, Poisson's ratio of υ=0.3. The geometry model used in numerical analysis is shown in Fig. 7. The maximum mesh size is controlled to within 1/10 shear wavelength at interest frequency to make sure numerical stability. Gabor wavelet is uniformly applied at the base of the model as a vertical shear wave in the form of stress, which has the following time history (Tripe et al. 2013):

$$s(t) = \sqrt{\alpha e^{-\beta t} t^{\gamma}} \sin(2 f \pi t) \tag{44}$$

where t is time, f denotes the central frequency of signal, α, β, γ are the parameters that dominate the signal feature such as amplitude, cycles, and decay rate. In this study, the values of α, β, γ are set to 6.5, 6.5, 5.0, while the true frequency f varies from 1.0Hz, 3Hz, 5Hz, 7Hz, 10Hz, and 15Hz. Free field boundary and quiet boundary are applied to the lateral and bottom boundaries for simulating a non-refection condition. The numerical displacement histories of well-soil system at various positions can be obtained as shown in Fig. 8. The results show that the peak displacement of free-field soil is amplified by around 40% while the peak displacement at the well top is impaired by around 75% compared to the bedrock displacement. Based on the definition of kinematic response in Eq. 42, the amplitude of I_u at f=15Hz is around 0.18.

Fig. 9 illustrates the kinematic response factor I_u of a seismic well derived from this present solution alongside numerical results. It is evident that the present solution generally aligns with the trends observed in the numerical results. Specifically, a well-soil system with greater modulus ratio (E_p/E_s) exhibits a more rapid attenuation as frequency increases. The present solution for E_p/E_s=1000 slightly underestimates the kinematic response factor. This discrepancy arises from the assumption that the decay function $\phi(r)$ is exclusively influenced by the radial distance to the well axis. In reality, the wave scattering occurs in three-dimensional directions, particularly when the disparity in wave speeds between the soil and the well is not sufficiently pronounced. Consequently, the model does not fully account for the radiation damping associated with the dissipation of stress wave energy in the vertical direction. Nevertheless, the current solution offers a rapid estimation of the seismic response of a well subjected to waves across a typical frequency range, which can be achieved within minutes. In contrast, obtaining comparable results through three-dimensional simulations under equivalent computational configurations may require several days.

Kinematic response and monitoring error of the downhole seismometer

Effects of soil-well modulus ratio E_p/E_s

Fig. 10 and Fig. 11 show the variations of frequency dependent kinematic response factor I_u and monitoring error with various modulus ratios, respectively. It can be seen in Fig. 10 that the peak value of I_u slightly increases from 1.20 to 1.24 as E_p/E_s increases from 200 to 10000. Considering the fact that such a modulus ratio range is quite broad in practical engineering applications, it can be deduced that peak values are not significantly influenced by changes in modulus ratio. By contrast, the critical frequency where I_u=1 decreases as the values of E_p/E_s increases. Moreover, larger values of E_p/E_s lead to a more rapid decline of I_u with frequency during the post-peaking stage. This phenomenon indicates that the seismometer wells in stiff soil are susceptible to heightened seismic responses across a wider frequency spectrum.

The results in Fig. 11 show that the signal error significantly fluctuates with varying frequencies. When the non-dimensional frequency a_0 is equal to zero, the responses of the seismometer at various depths closely resemble the bedrock response, resulting in a minimal signal error. An interesting observation is that the monitoring error follows a pattern of initially increasing to a positive peak, then sharply declining to a more pronounced negative peak. These impulse waves persist as the frequency increases, with the positive and negative peak values of subsequent waves being notably smaller than those of the initial waves. When the non-dimensional frequency a_0 approaches 2.0, the fluctuations in amplitude become imperceptible, and the error stabilizes at a constant negative value. Notably, the stable error magnitudes decrease as the modulus ratio increases. For the case of E_p/E_s=10000, the stable absolute error remains above 20%. Additionally, it is observed that the modulus ratio has a minimal impact on the first impulse wave but significantly influences subsequent waves. With the exception of the first impulse wave, a higher modulus ratio results in a smaller signal error, as depicted in Fig. 11.

Effects of slender ratio L_1/d

Fig. 12 and Fig. 13 show that the variations of frequency-dependent kinematic response factor I_u and signal error, respectively, across across installation depths of several tens of meters. The results in Fig. 12 show that the peak value of I_u is not sensitive to the installation length. For the case of L_1/d=5, the frequency corresponding to the peak value of I_u is marginally higher compared to other cases. Additionally, the kinematic response factors for L_1/d=10, 15 and 20 demonstrate minor discrepancies. Consequently, an embedded depth of 10*d* appears to be a critical threshold that determines the influence of installation depth on the kinematic response factor. This observation can be attributed to the concept of the active length L_a beyond which the soil deformation has an insignificant impact on the pile-head motion. Previous studies by Iovino et al. (2019) and Laora and Sanctis. (2013) have indicated that the value of L_a is the order of 10*d*, aligning well with the outcomes depicted in Fig. 12.

The results in Fig. 13 suggest that slender ratio L_1/d has a discernible impact on the signal error. The maximum errors typically manifest in the low-frequency range of a_0<0.2. For the case of L_1/d =5, the initial negative peak of the signal error reaches approximately 100%, slightly surpassing the positive peak at around 80%. As frequency increases, the subsequent peaks diminish significantly compared to those of the initial impulse, suggesting rapid attenuation of fluctuations with frequency. By contrast, for the cases of L_1/d =10, 15 and 20, multiple impulse waves are observed before reaching a stable state. It is also interesting that obvious reduction of peak error is observed as the slender ratio L_1/d increases from 10 to 15. Besides that, the frequencies at which peak errors occur vary, even when the embedded depth exceeds the active length L_a (10*d*). On the other hand, the ultimate stable values of error for all cases with various slender ratios are relatively similar. By integrating the observations in Fig. 12 and Fig. 13, it can be deduced that the signal error displays a higher sensitivity level compared to the kinematic response factor. The slender ratio or the embedded depth of a seismic well significantly influences the peak error, while exerting minimal impact on stable error values.

Fig. 14 shows the variations of the kinematic response factor (I_u) and monitoring error against non-dimensional frequency for the deep borehole. It can be observed that the variation of I_u for a deep borehole is similar with that for a shallow well. Notably, deep boreholes demonstrate smaller errors compared to their shallow counterparts. For the case of borehole depth L_1=100m, the maximum error is around 20%. As L_1 increases to 200m, the maximum error decreases to around 10%. Also notes that the signal error in the deep borehole does not vanish as frequency increases.

Signal error and displacement variation due to soil-well interaction

The relative disparity in displacement responses at the depth of L_1 and H within the free field soil is defined as the free field error, which can be quantified using the following calculation method:

$$E_{\mathrm{r}} = \frac{u_{L1} - u_{\mathrm{H}}}{u_{\mathrm{H}}} = \frac{\cos(\lambda_f L_1)}{\cos(\lambda_f H)} - 1 \tag{45}$$

In the presence of seismometer well, the responses at the depth of L_1 and H would be altered due to wave diffusion effects. To provide an explicit understanding of well-soil interaction, the response differences between u_{L1} and and u_{H} in the free field soil (or without well) and in the presence of seismometer well are calculated through Eq. (45) and Eq. (43), respectively. The results are plotted against dimensionless frequency in Fig. 15. Fig. 15(a) shows that the signal errors from the Eq. (43) and Eq. (45) have no significant difference for a_0<0.4, which reflects that the curvature of well foundation follows that of free field soil at low frequencies. As a_0 increases, the fluctuation magnitude of free field error gradually exceeds that of the true signal error. Moreover, the results considering well-soil interaction exhibit a tendency towards stability, while those in free field soil show a continuous upward trend. Similar trends are found in Fig. 15(b) and

Fig. 15(c). If we assume the motion of well and free field soil are identical at the same depth, i.e., $u_{\mathrm{p1}}(z)=u_{\mathrm{f}}(z)$, $u_{\mathrm{p2}}(z)=u_{\mathrm{f}}(z)$. It is found that the specific solution can satisfy boundary conditions in Eq. 20(a), Eq. 20(b), Eq. 31(a), Eq. 31(b), Eq. 31(e)- Eq. 31(h). For the continuous shear stress condition at well bottom in Eq. 31(c), it satisfies only when a_0=0; for the continuous moment condition at well bottom in Eq. 31(d), it produces the equation: $\lambda^3{}_{\mathrm{f}}=(G_{\mathrm{s}}^{*}A_{\mathrm{p2}})/(E_{\mathrm{p2}}^{*}I_{\mathrm{p2}})$.Combining the definition of $\lambda_{\mathrm{f}}^{2}=\rho_{\mathrm{s}}\omega^{2}/G_{\mathrm{s}}^{*}$, one can find that the specific solution exists only when the value of a_0 meets the following:

$$a_0=d\left(\frac{G_{\mathrm{s}}^{*}A_{\mathrm{p2}}}{E_{\mathrm{p2}}^{*}I_{\mathrm{p2}}}\right)^{1/3} \tag{47}$$

Therefore, it can be found that the 'specific solution' of $u_{\mathrm{p1}}(z)=u_{\mathrm{f}}(z),u_{\mathrm{p2}}(z)=u_{\mathrm{f}}(z)$ does not exist because the boundaries of Eq. 31(c) and 31(d) cannot be satisfied simultaneously. Nevertheless, the dimensionless frequency determined by Eq. (47) serves as a possible indicator of a critical threshold at which the signal error may be approximated by the free field error. For the given cases in Fig. 15, as it is found that the true signal error by Eq. (43) agrees well with the free field error by Eq. (45) in the range of $a_{\mathrm{o}}<a_{\mathrm{cri}}=0.175$. For the higher frequencies, it is essential to conduct a thorough assessment of monitoring error using the present method by Eq. (43).

Fig. 16 and Fig. 17 show the comparisons of displacement profiles with depth for free field soil and well-soil systems across various frequencies for $L_1=15d$ and $L_1=5d$, respectively. The foundation thickness of seismometer well is a constant of $1d$, and the bedrock depth L is set to $100d$ in both Fig. 16 and Fig. 17. The results depicted in Fig. 16(a) highlight the notable influence of frequency on displacement variations with depth. Higher frequency generally leads to shorter wavelengths and reduced amplitudes. In the case where a_0=0, the soil-well system exhibits rigid body behavior, resulting in displacement patterns mirroring those of the bedrock. At a_0=0.054, the soil at the ground surface moves in the same direction as the bedrock but with a greater amplitude. At a_0=0.162, the soil motion at the ground surface exhibits an opposite direction to that at the bedrock, with an approximate amplitude of $0.55u_{\mathrm{g}}$. As the frequency increases, the displacement at the ground surface diminishes rapidly, while the displacement near the bedrock remains significant. Additionally, displacement amplitude exhibits an upward trend with increasing depth, particularly for medium to high frequencies such as a_0=0.406, 0.704 and 0.950. This behavior can be attributed to the rapid attenuation of high-frequency waves, leading to a concentration of energy in a limited zone above the bedrock as frequency rises. In Fig. 16(b), minimal variation in soil displacement below the well is observed. Fig. 16(c) compares the displacement of a well and the displacement of the free field soil within a depth range from 0 to H when L_1=15d. The analysis reveals that the curvature of well displacement is stiffer than that of free field soil near the ground surface and at the well's base. The difference of u/u_g resulting from the well-soil interaction decreases as distance increases from these particular locations.

The detailed results in Fig. 17 show the variation in displacement from z=0 to z=H with and without the well for different frequencies when L_1=5d. In comparison to Fig. 16(c), the displacement curvature of the well when L_1=5d in Fig. 17 exhibits reduced flexibility than that when L_1=15d. Consequently, more pronounced disparities between the displacement characteristics of free field soil and downhole well near the ground surface and well bottom are observed when L_1=5d compared to L_1=15d. This observation can be attributed to the fact that short cylinders tend to rotate, while long cylinders tend to bend under transverse loading conditions.

Ground displacement around downhole well

The spatial distribution of energy within the soil-well system is intricate due to the interaction between the soil and the well. Fig. 18 shows the contours representing the dimensionless transverse displacement of the soil-well system at different frequencies. The transverse displacement u_s is determined with Eq. (1) and normalized with respect to the free field displacement at the ground surface. The normalization is divided into two sections: the range of normalized depth from 0 to 1.0 corresponds to the hollow section of the downhole well and its surrounding soil, while the range from 1.0 to 1.2 corresponds to the foundation section and its surrounding soil.

As the radial distance increases, the dimensionless transverse displacement for z=0 in Fig. 18 approaches unity at approximately r=10 R_o for low frequencies and even before 10 R_o for medium to high frequencies. Additionally, the contour lines become denser with increasing frequency, indicating the variation in wave propagation speed with frequency. Specifically, in regions with positive displacement, contour lines with a downward convex shape signify displacement attenuation as r increases, while those with an upward convex shape indicate displacement amplification. For regions with negative displacement, these features are reversed. Degree of convexity can indicate the rate of attenuation. It can be found that the displacement attenuation is rapid near the ground surface in the vicinity of well in Fig. 18(a), Fig. 18(b) and Fig. 18(c). Furthermore, the concavity or convexity of the contours may vary with depth, which is associated with the wave propagation in the z direction. In Fig. 18(c) for $\omega d/V_s$=0.8, the enclosed area by contour lines of -0.8 and -1.0 experiences significant vibration and represents an energy accumulation zone in this soil-well system. Moreover, contour plots can reflect variations in displacement within the well foundation, aiding in the estimation of monitoring errors.

7 Discussion and conclusions

This paper introduces a viscoelastic solution that addresses the transverse kinematic response of a downhole seismometer to S-waves. Deformation of the soil-well system is considered within a small strain range to facilitate the calculation of the whole system's energy under assumption of viscoelastic media. The solution is derived through the application of variational analysis and Hamilton's principle in the frequency domain. The primary constraints of this study are the omission of soil heterogeneity and nonlinearity, as well as the idealization of seismic action as a harmonic wave. The impact of realistic soil strata and anisotropy is not considered in this present solution. The transverse displacement is modeled without considering potential coupling effects between transverse and longitudinal motions. Further research efforts will focus on overcoming these limitations to attain a more feasible solution for addressing relevant serviceability issues. Additionally, the current methodology does not impose any depth constraints, thus facilitating the analysis of the responses from deep boreholes, e.g. the KiK-net downhole arrays. However, when employing this model, it is essential to take into account the compatibility of the installation method. The main conclusions can be summarized as follows:

(a) The kinematic response factor of downhole wells may exceed one, i.e., amplification occurs, within the common frequency range of $0<\omega d/V_s<1$. The lower modulus ratio of well-to-soil leads to a broader amplification range.

(b) The accuracy of downhole seismometer is significantly affected by the geometrics of the well, the stiffness of soil, and the frequency of seismic wave. The trend observed in signal error across different frequencies bears resemblance to the configuration of a multi-impulse waveform. Specifically, the amplitude of both the positive and negative peaks within the initial impulse surpasses that of subsequent impulses. It is noteworthy that the signal errors detected in deep boreholes are generally smaller than those encountered in shallow boreholes.

(c) As the frequency rises, the signal error may decrease to a consistent level but will not completely disappear. In contrast, the results from free field analysis, which excludes influence of soil-well interaction, demonstrate a consistent increase in relation to frequency. Therefore, utilizing free field motion for estimating signal error is primarily suitable for low frequencies.

Data Availability Statement

The theoretical and numerical data developed for the dynamic response of a soil-well system are available from the corresponding author upon reasonable request.

Acknowledgements

This research was financially supported by the National Natural Science Foundation of China (No:52208370); the Fundamental Research Funds for the Central Universities (No:2682024CX085); We also appreciate the support from interdisciplinary innovation team of Southwest Jiaotong university.

Notation

r, θ, z coordinate axis

R_o, R_i, d outside radius, internal radius and outside diameter of the downhole well

L total thickness of the soil layer

H total length of the downhole well

L_1, A_{p1}, I_{p1} length, cross section area and second moment of area for the hollow section of the downhole well

L_2, A_{p2}, I_{p2} length, cross section area and second moment of area of well foundation

L_3, A_{p3} thickness and cross section area of the substratum soil column

E_p, ρ_p Young's modulus and mass density of downhole well

E_s, ρ_s, V_s Young's modulus, mass density and shear velocity of soil

υ_s, κ_s Poisson's ratio and hysteretic damping ratio of soil

λ_s^*, G_s^* Complex Lame's constants

E_s^* Complex Young's modulus

u_{pi} transverse displacement of the well and the fictitious soil column

u_{si}, v_{si}, w_{si} displacement components of soil

t time

ω circular frequency

a_0 dimensionless frequency, $a_0 = \omega d / V_s$

E_r signal error

I_u kinematic response factor under S-wave

u_g displacement amplitude of the bedrock

u_f free field displacement under vertically incident S-waves

U_f relative displacement of free field with respect to the bedrock

A, B, D, F coefficients for determining the displacement of well-soil system

λ_f parameter for free-field displacement

σ, τ normal and shear stess

ε, γ normal and shear strain

Π strain energy

T kinetic energy

$\Re$ energy function

δ calculus of variation

$f_{ji}(z), j=1,2,3,4$ solution functions for the downhole well

$c_{ji}, \lambda_i^j, j=1,2,3,4$ coefficients for the downhole well

ϕ decay function of displacement

$k, \xi, \alpha, \beta, \vartheta, \varsigma, q, \chi_{pi}, \psi_i$ temporary coefficients

References

Anoyatis, G., Laora, R.D., Mandolini, A., and Mylonakis, G. 2013. “Kinematic response of single piles for different boundary conditions: analytical solutions and normalization schemes.” *Soil Dyn Earthq Eng* 44:183–195. https://doi.org/10.1016/j.soildyn.2012.09.011.

Basu, D., Prezzi, M., Salgado, R., and Chakraborty, T. 2008. “Settlement analysis of piles with rectangular cross sections in multi-layered soils.” *Comput Geotech* 35: 563-575 https://doi.org/10.1016/j.compgeo.2007.09.001.

Chen, L.B., Li, J.X., Wu, W.B., Liu, H., Yao, Y., and Zhang, P. 2023. “New method to calculate the kinematic response of offshore pipe piles under seismic S-waves.” *Soil Dyn Earthq Eng* 165: 107651. https://doi.org/10.1016/j.soildyn.2022.107651.

Cui, C.Y., Liang, Z.M., Xu, C.S., Xin, Y., and Wang, B.L. 2023. “Analytical solution for horizontal vibration of end-bearing single pile in radially heterogeneous saturated soil.” *Appl. Math. Model* 116:65–83. https://doi.org/10.1016/j.apm.2022.11.027.

Eisner, L., Hulsey, B.J., Duncan, P., Jurick, D., Werner, H., and Keller, W. 2010. “Comparison of Surface and borehole locations of induced seismicity.” *Geophys Prospect* 58(5):809–820. https://doi.org/10.1111/j.1365-2478.2010.00867.x.

Fan, K., Gazetas, G., Kaynia, A., Kausel, E., and Ahmad, S. 1991. “Kinematic seismic response of single piles and pile groups.” *Int J Geotech Eng* 117(12):1860-1879.

https://doi.org/10.1061/(ASCE)0733-9410(1991)117:12(1860).

Fang, S.J., Huang, R.Q., Guo, W., He, C., Jiang, L.Z., Yu, Z.W., Wang, Y., Zeng, C., Liang GY, and Yang S. 2023. “Safety speed threshold of high-speed train running on bridges under seismic excitation of different soil types.” *Structures* 58(12): 105429. https://doi.org/10.1016/j.istruc.2023.105429

Guo, W.D., and Lee, F.H. 2001. “Load transfer approach for laterally loaded piles.” *Int J Numer Anal Methods Geomech* 25:1101-1129. https://doi.org/10.1002/nag.169.

Gazetas, G. 1984. “Seismic response of end-bearing single piles.” Soil Dyn Earthq Eng 3(2): 82-93. https://doi.org/10.1016/0261-7277(84)90003-2

Hardin, B.O., and Drnevich, V.P. 1972. “Shear modulus and damping in soils: design equations and curves. Journal of the Soil” *mechanics and Foundations Division* 98(7):667-692. https://doi.org/10.1061/JSFEAQ.0001760

Horiuchi, S., Horiuchi, Y., and Yamamoto, S. 2009. “Home seismometer for earthquake early warning.” Geophys Res Lett 36: L00B04. https://doi.org/10.1029/2008GL036572.

He, R., Kaynia, A.M., Zhang, J.S., and Chen, W.Y. 2020. “Seismic response of monopiles to vertical excitation in offshore engineering.” *Ocean Eng* 216: 108120. https://doi.org/10.1016/j.oceaneng.2020.108120.

Hollender F, Theodoulidis N, Mariscal A, Chaudat T, Steidl J, Pierre YB; Roumelioti Z. 2023. “The "Glass Beads" coupling solution for borehole and posthole accelerometers: shaking table tests and field retrievability. Seismol.” *Res. Lett*. 94(2A): 925–934. https://doi.org/10.1785/0220220292.

Iovino, M., Di, Laora.R., Rovithis, E., and Sanctis, L.D. 2019. “The Beneficial role of piles on the seismic loading of structures.” *Earthq Spectra* 35(3):1141-1162. https://doi.org/10.1193/061318EQS146M.

Ke, W.H., and Zhang, C. 2017. “A closed-form solution for kinematic bending of end-bearing piles.” *Soil Dyn Earthq Eng* 103:15–20. https://doi.org/10.1016/j.soildyn.2017.09.004.

Ke, W.H., Liu, Q.J., and Zhang, C. 2019. “Kinematic bending of single piles in layered soil.” *Acta Geotech* 14:101–110. https://doi.org/10.1007/s11440-018-0640-y.

Laora, R.D., and Sanctis, L.D. 2013. “Piles-induced filtering effect on the foundation input motion.” *Soil Dyn Earthq Eng* 46: 52–63. https://doi.org/10.1016/j.soildyn.2012.12.007.

Liu, Q.J., Deng, F.J., and He, Y.B. 2014. “Transverse seismic kinematics of single piles by a modified

Vlasov model.” *Int J Numer Anal Methods Geomech* 38:1953–1968. https://doi.org/10.1002/nag.2286.

Laora, R.D., and Rovithis, E. 2015. “Kinematic bending of fixed-head piles in nonhomogeneous soil.” *J Geotech Geoenviron* 141(4): 04014126. https://doi.org/10.1061/(ASCE)GT.1943-5606.0001270.

Lin, Y.Y., Chen, D.Y., Kuo, C.H., Lin, C.J., Chen, W.Y., and Wen, Y.Y. 2022. “Orientation corrections of a borehole seismometer network in Taiwan using teleseismic earthquakes.” *Seismol Res Lett* 93: 1532–1548. https://doi.org/10.1785/0220210248.

Lee, H., and Sheen, D.H. 2015. “A study on determination of orientation of borehole seismometer.” *J Geol Soc Korea* 51: 93–103. https://doi.org/10.14770/jgsk.2015.51.1.93

Mylonakis, G. 2001. “Elastodynamic model for large-diameter end-bearing shafts.” *Soils Found* 41(3):31–44. https://doi.org/10.3208/sandf.41.3_31.

Nikolaou, S., Mylonakis, G., Gazetas, G., and Tazoh, T. 2001. “Kinematic pile bending during earthquakes: analysis and field measurements.” *Geotechnique* 51: 425–440. https://doi.org/10.1680/geot.2001.51.5.425.

Payan, M., Senetakis, K., Khoshghalb, A., and Khalili, N. 2016. “Influence of particle shape on small-strain damping ratio of dry sands.” *Geotechnique* 66(7): 610-616. https://doi.org/10.1680/jgeot.15.T.035.

Prevedel, B., Bulut, F., Bohnhoff, M., Raub, C., Kartal, R.F., Alver, F., and Malin, P.E. 2015. “Downhole geophysical observatories: best installation practices and a case history from Turkey.” *Int J Earth Sci* 104:1537–1547. https://doi.org/10.1007/s00531-015-1147-5.

Pilz, M. and Cotton, F. 2019. “Does the one-dimensional assumption hold for site response analysis? A study of seismic site responses and implication for ground motion assessment using Kik-net strong-motion data.” *Earthquake Spectra* 35(2): 883-905. DOI: 10.1193/050718EQS113M.

Qu, L.M., Yang, C.W., Ding, X.M., Kouroussis, G., and Zheng, C.J. 2021a. “A continuum-based model on axial pile-head dynamic impedance in inhomogeneous soil.” *Acta Geotech* 16: 3339-3353. https://doi.org/10.1007/s11440-021-01274-x.

Qu, L.M., Yang, C.W., Ding, X.M., Kouroussis, G., and Yuan, C. 2021b. “Vertical vibration of piles with square cross-section.” *Int J Numer Anal Methods Geomech* 45(18): 2629-2653. https://doi.org/10.1002/nag.3280.

Rovithis, E.N., Parashakis, H., and Mylonakis, G.E. 2011. “1D harmonic response of layered inhomogeneous soil: analytical investigation.” *Soil Dyn Earthq Eng* 31:879–890. https://doi.org/10.1016/j.soildyn.2011.01.007.

Somerville, P. 2022. “The Mw 7.3 Fukushima, Japan Earthquake of 16 March 2022.” *Risk Frontiers, Briefing Note* 463. http://doi.org/10.32858/temblor.246.

Seo, H., and Prezzi, M. 2007. “Analytical solutions for a vertically loaded pile in multilayered soil.” *Geomech and Geoengin* 2(1):51–60. https://doi.org/10.1080/17486020601099380.

Salgado, R., Seo, H., and Prezzi, M. 2013. “Variational elastic solution for axially loaded piles in multilayered soil.” *Int J Numer Anal Methods Geomech* 37(4):423-440. https://doi.org/10.1002/nag.1110.

Tripe, R., Kontoe, S., Wong, T.K.C. 2013. “Slope topography effects on ground motion in the presence of deep soil layers.” *Soil Dyn Earthq Eng* 31:879–890. https://doi.org/10.1016/j.soildyn.2013.02.011.

Thompson, D.J., Kouroussis, G., and Ntotsios, E. 2019. “Modelling, simulation and evaluation of ground vibration caused by rail vehicles.” *Vehicle Syst Dyn* 57(7): 936–983. https://doi.org/10.1080/00423114.2019.1602274.

Theodoulidis, N., Hollender, F., Mariscal, A., et al. 2018. “The ARGONET (Greece) seismic observatory: An accelerometric vertical array and its data.” *Seismol. Res. Lett.* 89, 1555–1565. https://doi.org/10.1785/0220180042.

Thompson, E.M., Baise, L.G., Kayen, R.E., et al. 2009. “Impediments to predicting site response: Seismic property estimation and modeling simplifications.” *Bulletin of the Seismological Society of America* 99(5): 2927-2949. https://doi.org/10.1785/0120080224.

Vallabhan, C.V.G., and Mustafa, G. 1996. “A new model for the analysis of settlement of drilled piers.” *Int J Numer Anal Methods Geomech* 20 :143-152. https://doi.org/10.1002/(SICI)1096-9853(199602)20:2<143:AID-NAG812>3.0.CO;2-U.

Yang, C.W., Zhang, K.W., Zhang, Z.F., Su, K., Qu, L.M., and Zhang, L. 2023a. “Fractal slope-based seismic wave detection method.” *B Seismol Soc Am* 113(6): 2311–2322. https://doi.org/10.1785/0120220220.

Yang, C.W., Yuan, C., Qu, L.M., and Ding, X.M. 2023b. “Analytical method for the kinematic response and signal error of a downhole seismometer subjected to P-waves.” *Soil Dyn Earthq Eng* 164:107645. https://doi.org/10.1016/j.soildyn.2022.107645.

Zheng, C.J., Luo, T., Kouretzis, G., Ding, X.M., and Luan, L.B. 2022. “Transverse seismic response of end-bearing pipe piles to S-waves.” *Int J Numer Anal Methods Geomech* 46:1919–1940. https://doi.org/10.1002/nag.3374.

Zhang, X., Zhang, M., and Tian, X. 2021. “Real-time earthquake early warning with deep learning: application to the 2016 M 6.0 Central Apennines, Italy Earthquake.” *Geophys Res Lett* 48(5): 2020GL089394. https://doi.org/10.1029/2020GL089394.

Zhang, Y.P., Liu, H., Wu, W.B., Wang, L.X., and Jiang, G.S. 2021. “A 3D analytical model for distributed low strain test and parallel seismic test of pipe piles.” *Ocean Eng* 225:108828. https://doi.org/10.1016/j.oceaneng.2021.108828.

Zhang, X.L., Peng, X.B., Chen, S.L., Li, X.J., Dou, Z., He, X.L., and Xu, C. 2021. “Rapid prediction of strong ground motions from major earthquakes: an example in the Wudu basin, Sichuan, China.” *B Seismol Soc Am* 111(5): 2635–2660. https://doi.org/10.1785/0120210066.

Figure 1

Figure 2

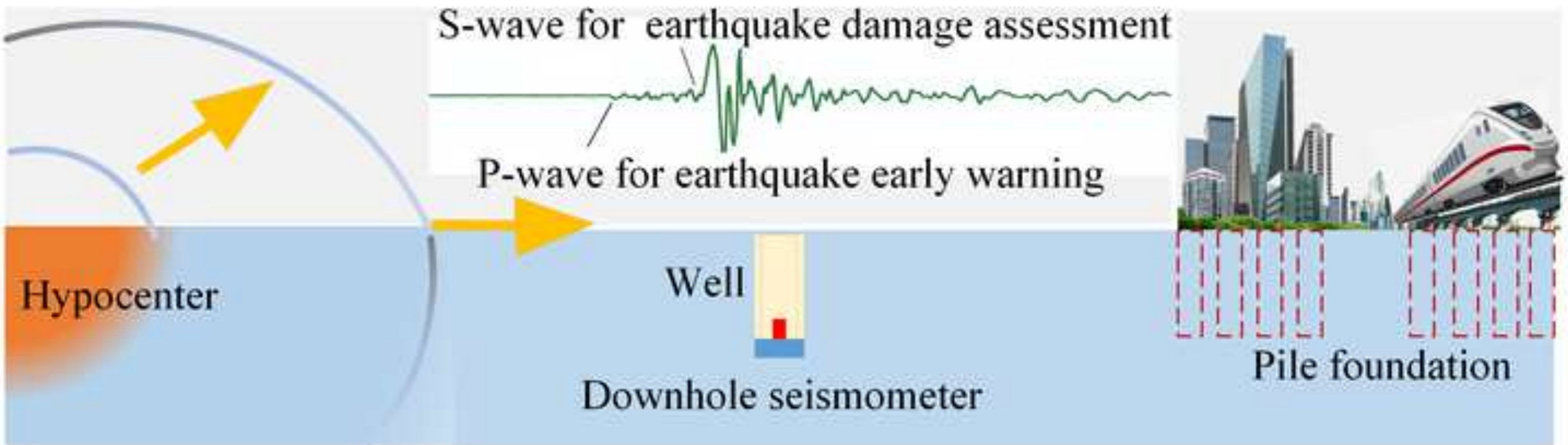
S-wave for earthquake damage assessment
P-wave for earthquake early warning
Hypocenter
Well
Downhole seismometer
Pile foundation

Figure 3

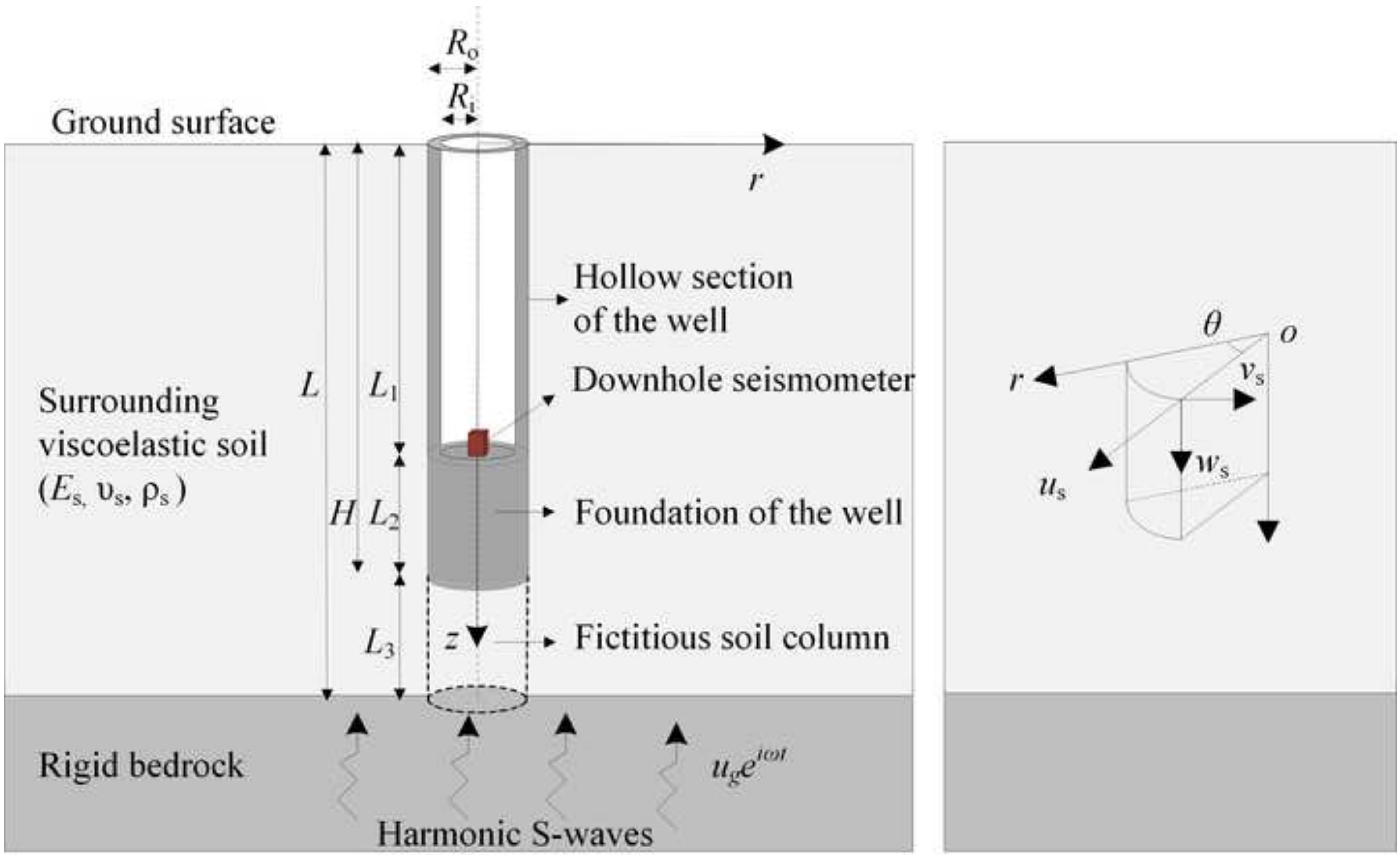

R_o
R_i
Ground surface
r
Hollow section of the well
Downhole seismometer
Surrounding viscoelastic soil
(E_s, υ_s, ρ_s)
L
L_1
H
L_2
Foundation of the well
L_3
z
Fictitious soil column
Rigid bedrock
$u_g e^{i\omega t}$
Harmonic S-waves
θ
o
r
v_s
u_s
w_s

Figure 4

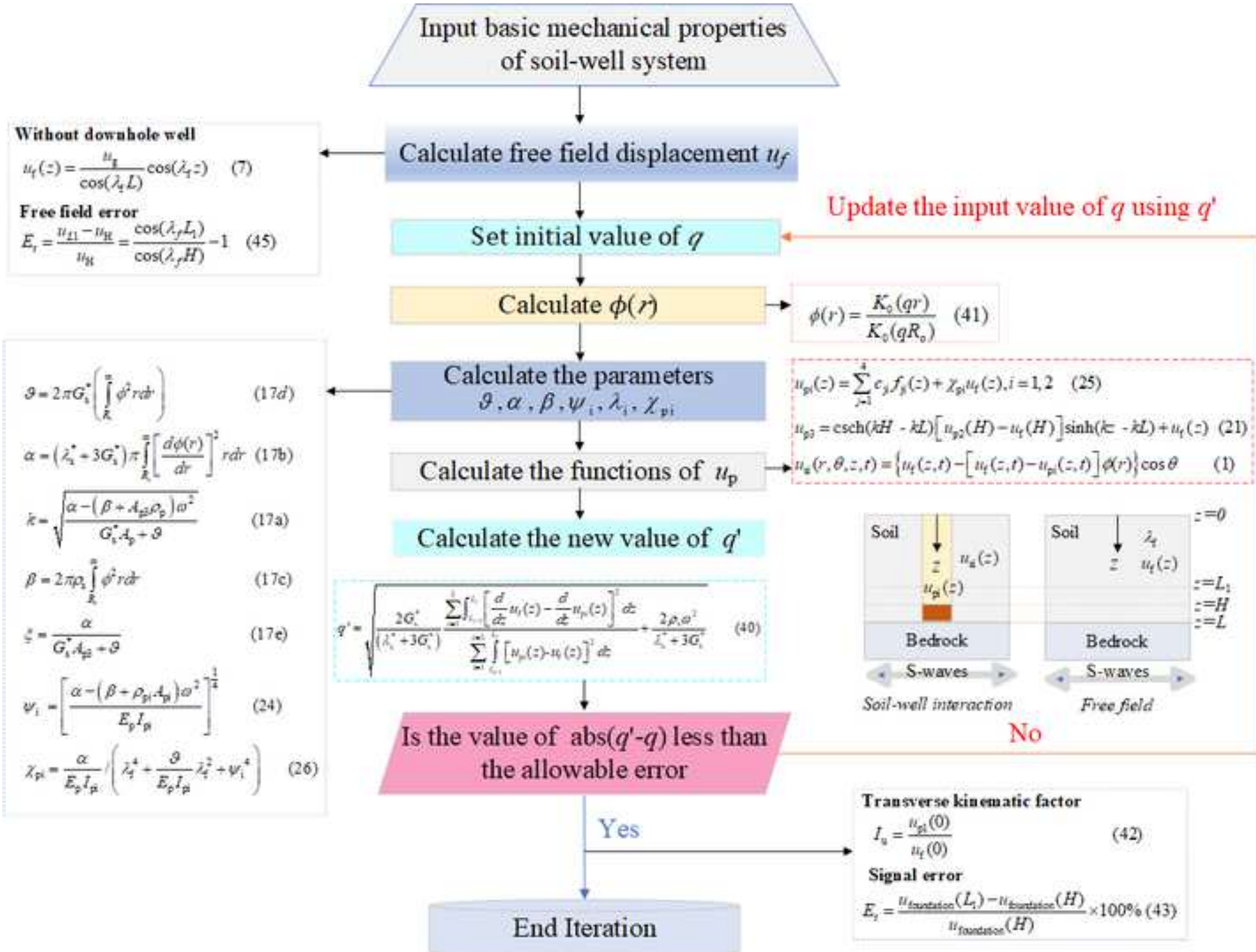
Input basic mechanical properties of soil-well system
Calculate free field displacement u_f
Without downhole well
Free field error
Set initial value of q
Update the input value of q using q'
Calculate $\phi(r)$
Calculate the parameters $\vartheta, \alpha, \beta, \psi_i, \lambda_i, \chi_{pi}$
Calculate the functions of u_p
Calculate the new value of q'
Soil
Bedrock
S-waves
Soil-well interaction
Free field
Is the value of abs(q'-q) less than the allowable error
No
Yes
Transverse kinematic factor
Signal error
End Iteration

Figure 5a

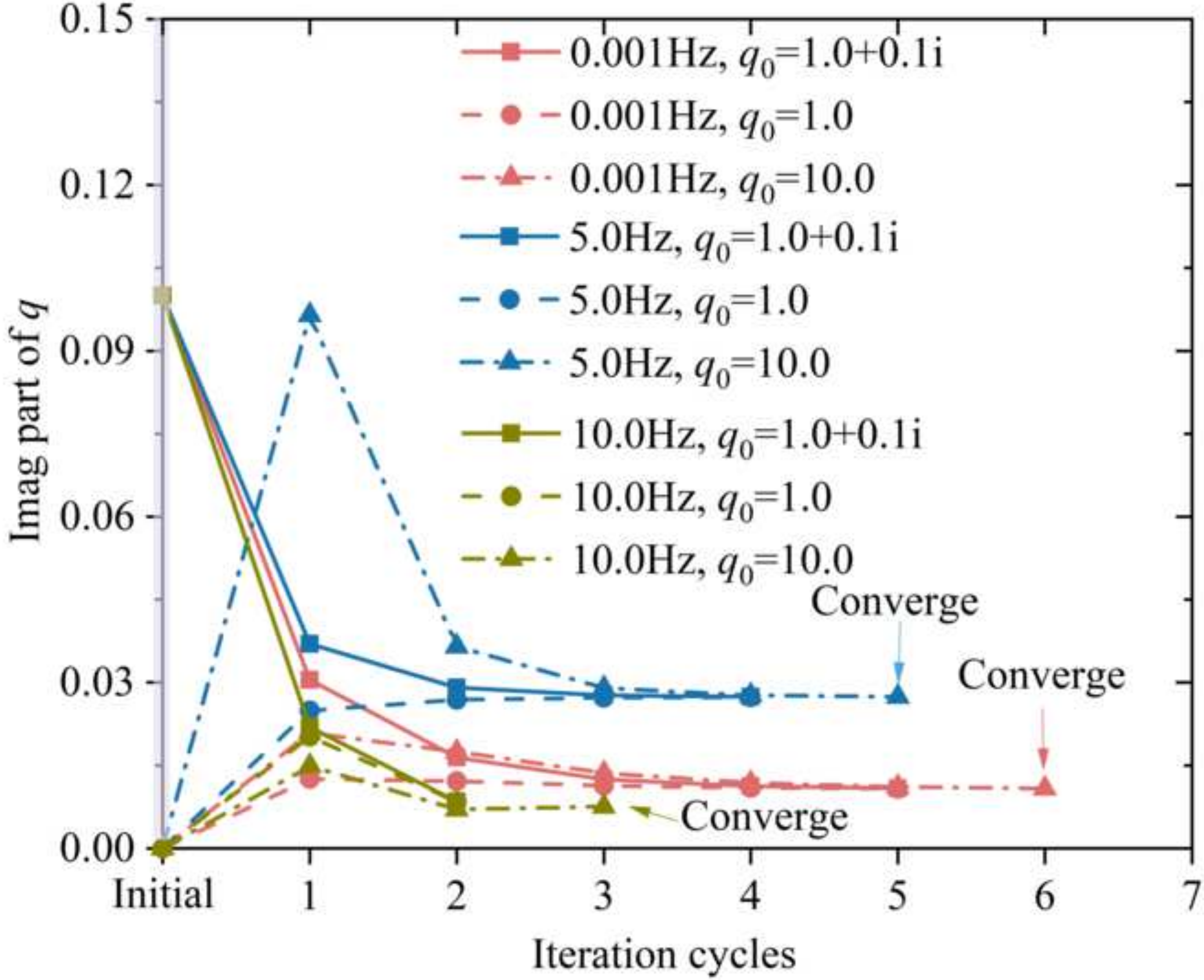
0.001Hz, q_0=1.0+0.1i
0.001Hz, q_0=1.0
0.001Hz, q_0=10.0
5.0Hz, q_0=1.0+0.1i
5.0Hz, q_0=1.0
5.0Hz, q_0=10.0
10.0Hz, q_0=1.0+0.1i
10.0Hz, q_0=1.0
10.0Hz, q_0=10.0
Converge
Converge
Converge
Imag part of q
0.15
0.12
0.09
0.06
0.03
0.00
Initial
1
2
3
4
5
6
7
Iteration cycles

Figure 5b

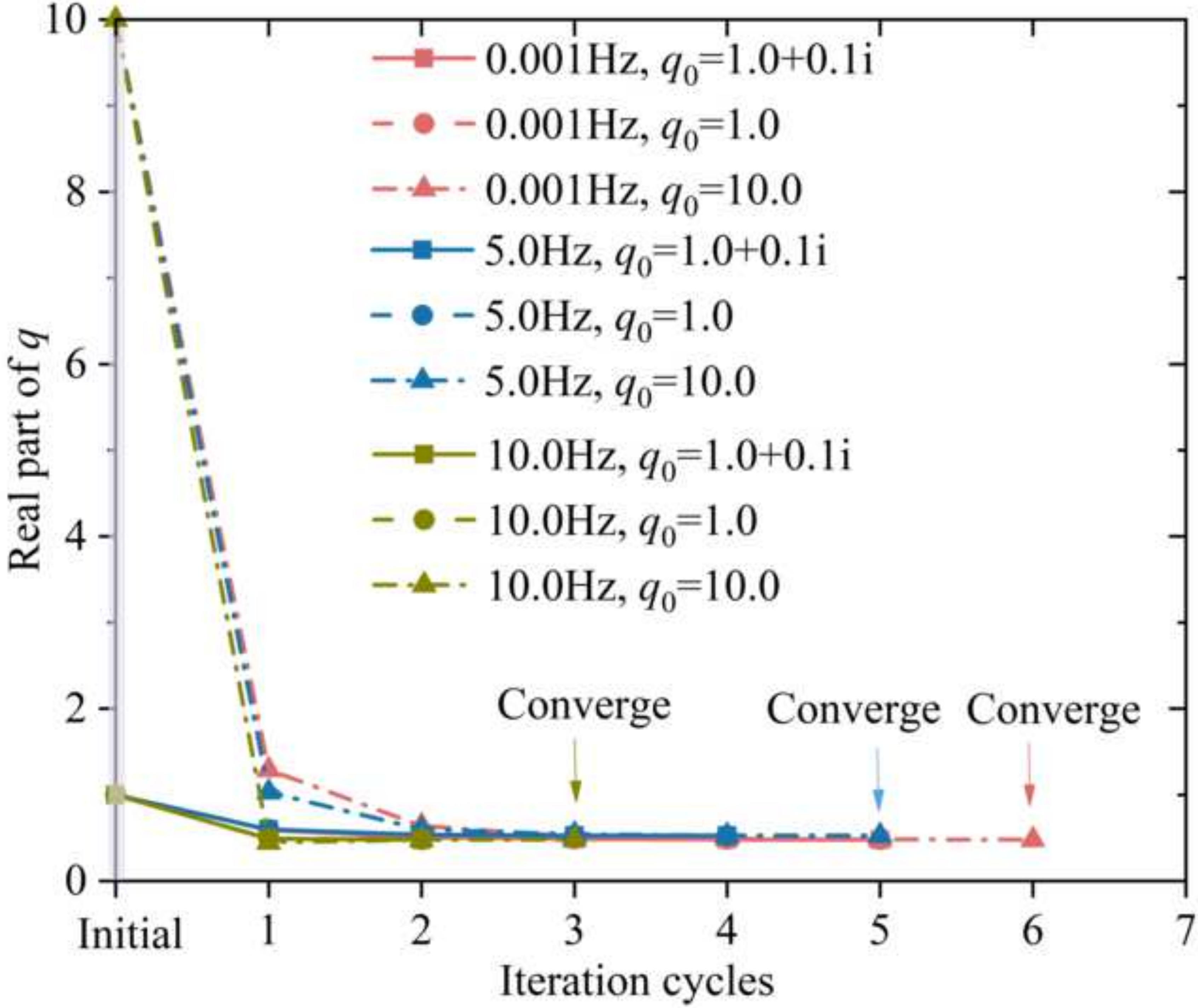

0.001Hz, q_0=1.0+0.1i
0.001Hz, q_0=1.0
0.001Hz, q_0=10.0
5.0Hz, q_0=1.0+0.1i
5.0Hz, q_0=1.0
5.0Hz, q_0=10.0
10.0Hz, q_0=1.0+0.1i
10.0Hz, q_0=1.0
10.0Hz, q_0=10.0
Converge
Converge
Converge
Real part of q
0
2
4
6
8
10
Initial
1
2
3
4
5
6
7
Iteration cycles

Figure 6

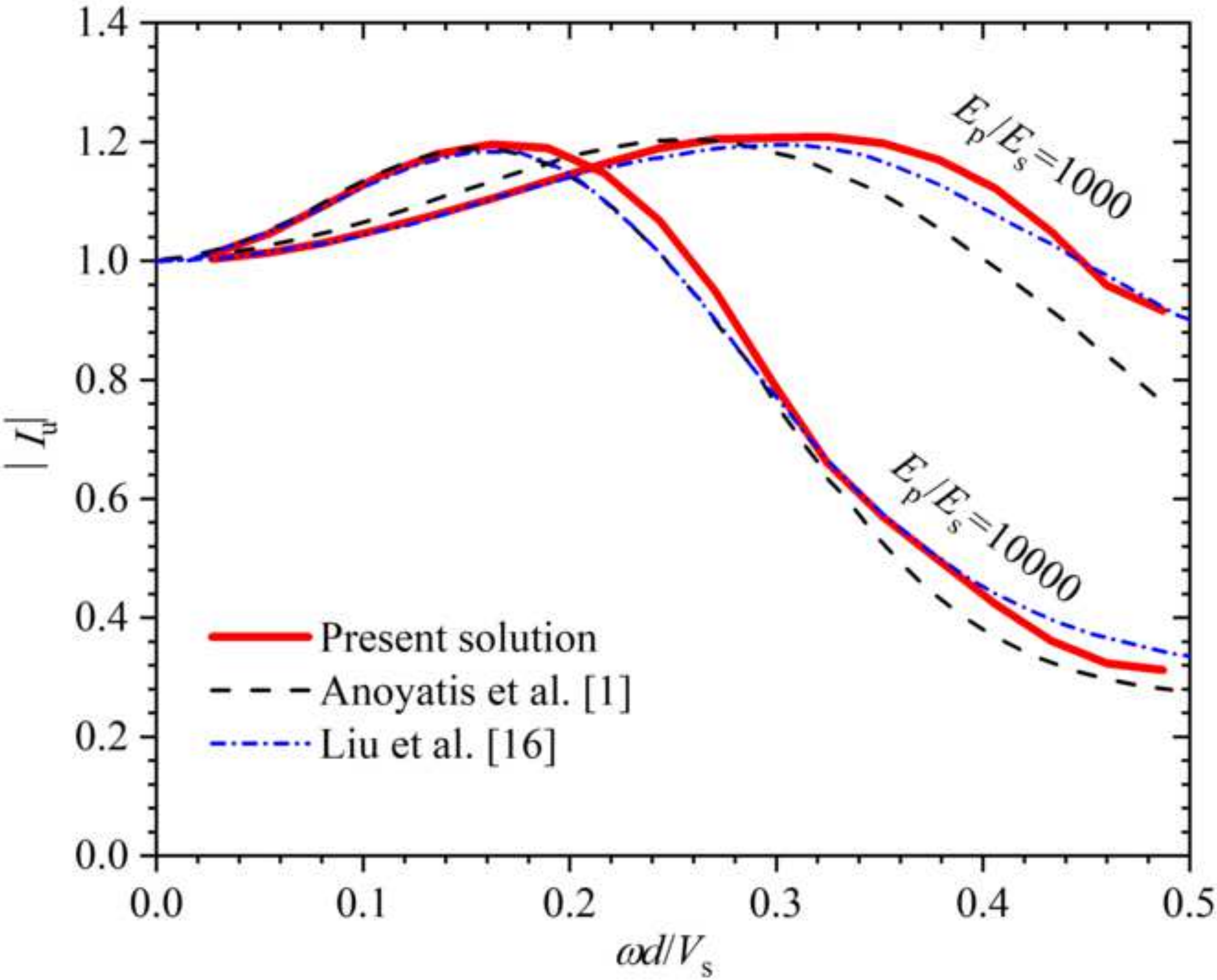

1.4
1.2
1.0
0.8
0.6
0.4
0.2
0.0
0.0
0.1
0.2
0.3
0.4
0.5
$|I_u|$
$\omega d/V_s$
$E_p/E_s=1000$
$E_p/E_s=10000$
Present solution
Anoyatis et al. [1]
Liu et al. [16]

Figure 6

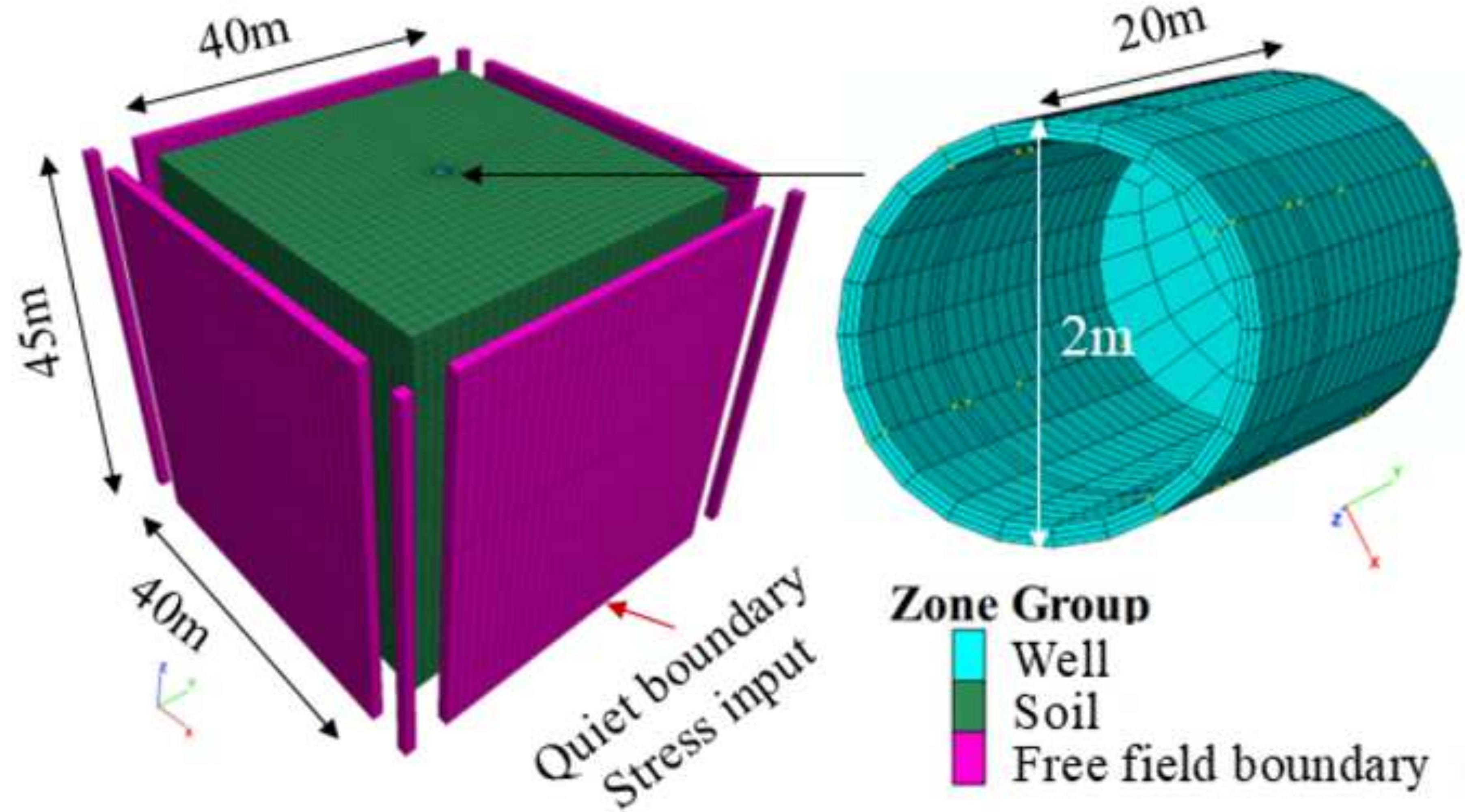
40m
45m
40m
20m
2m
Quiet boundary
Stress input
Zone Group
Well
Soil
Free field boundary

Figure 8

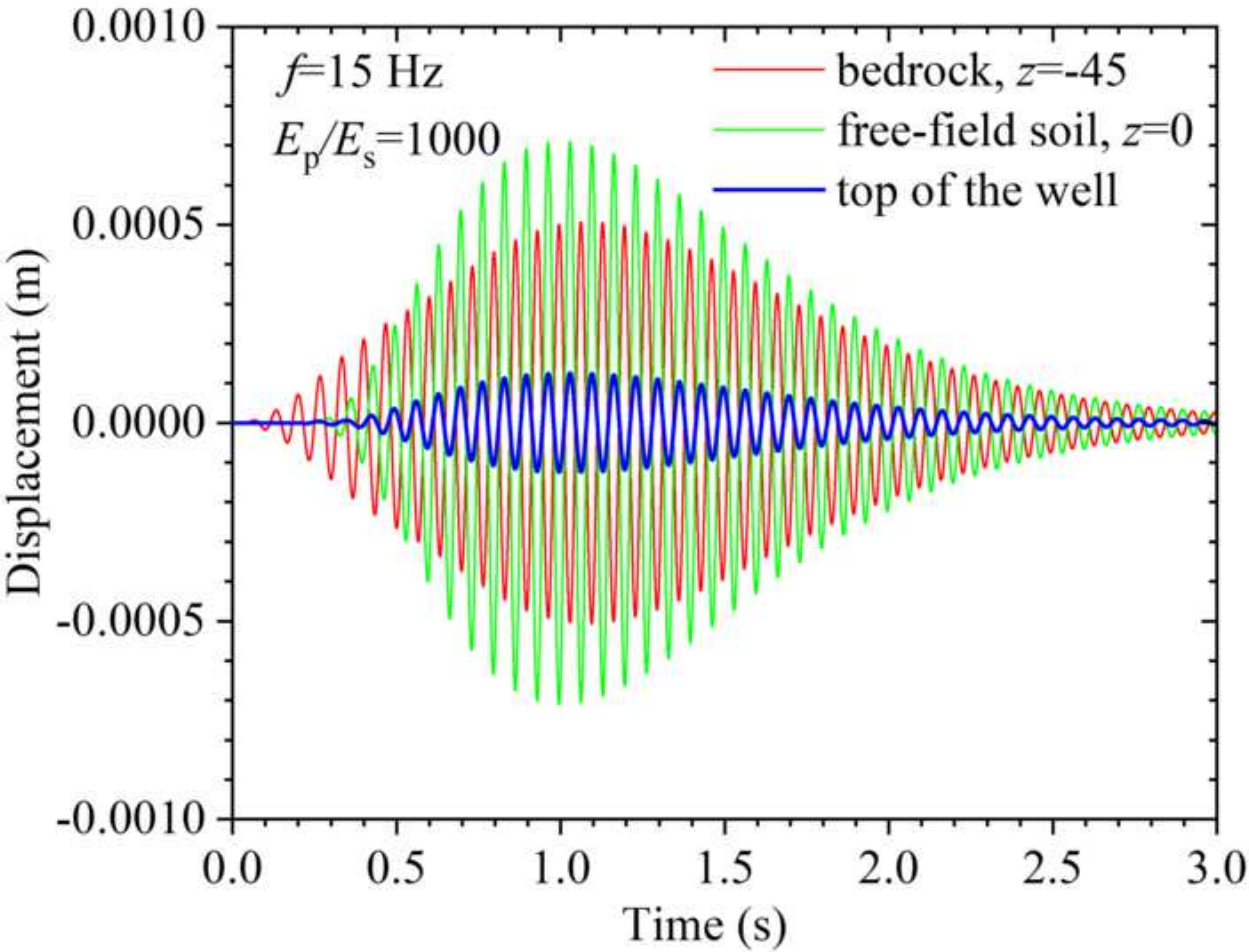

f=15 Hz
E_p/E_s=1000
bedrock, z=-45
free-field soil, z=0
top of the well
0.0010
0.0005
0.0000
-0.0005
-0.0010
Displacement (m)
0.0
0.5
1.0
1.5
2.0
2.5
3.0
Time (s)

Figure 9

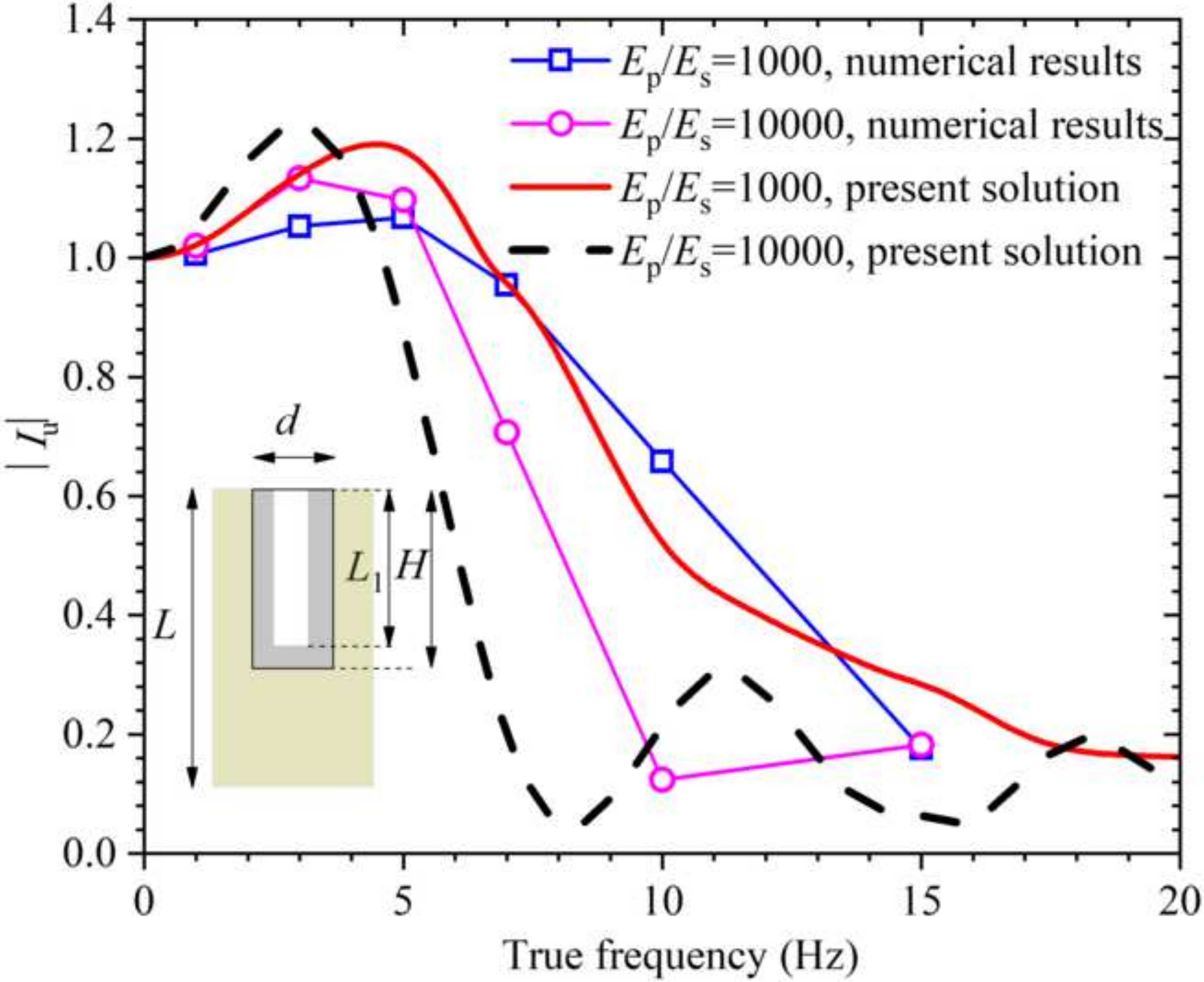

E_p/E_s=1000, numerical results
E_p/E_s=10000, numerical results
E_p/E_s=1000, present solution
E_p/E_s=10000, present solution
$|I_u|$
True frequency (Hz)
0
5
10
15
20
0.0
0.2
0.4
0.6
0.8
1.0
1.2
1.4
d
L
L_1
H

Figure 10

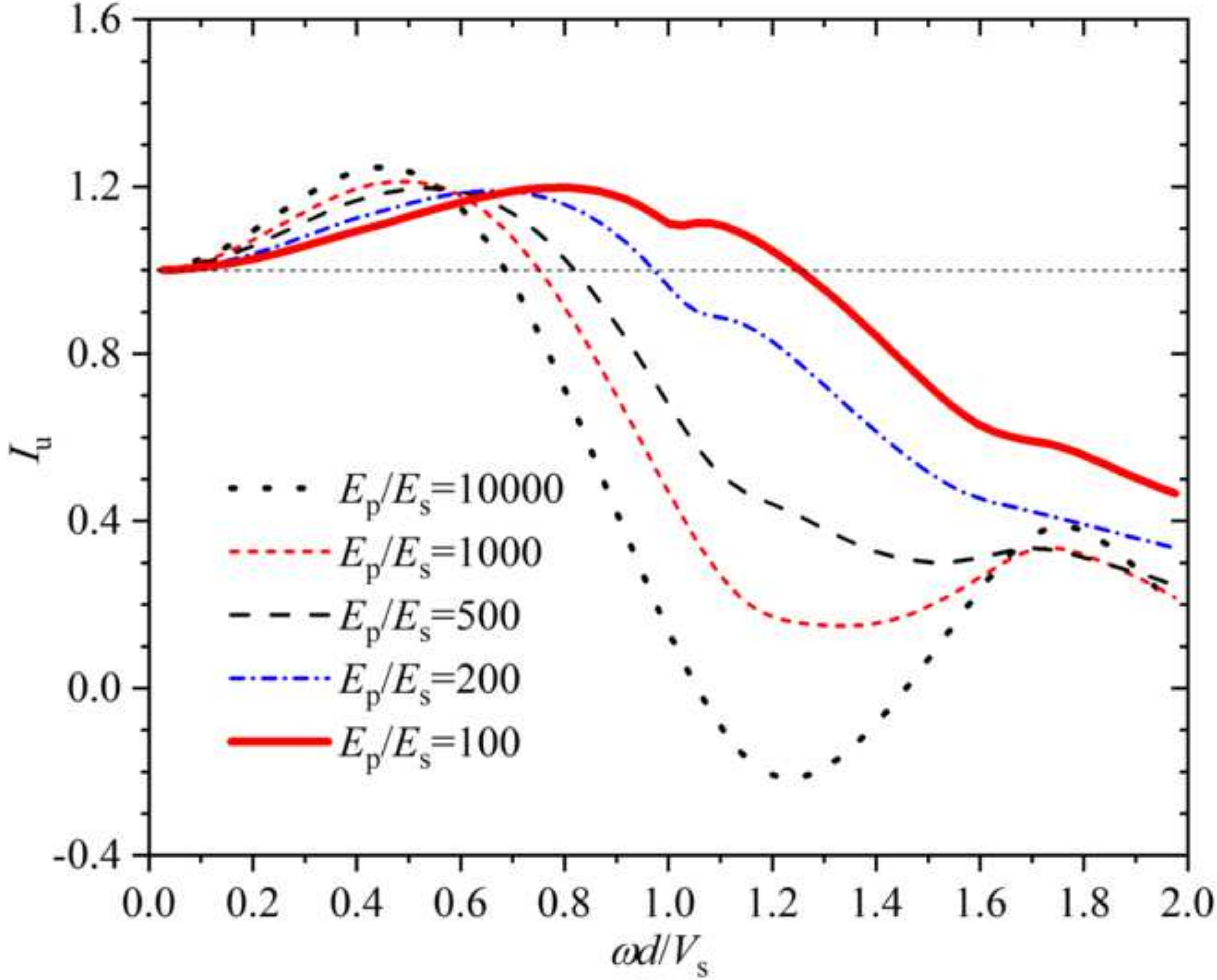
1.6
1.2
0.8
0.4
0.0
-0.4
0.0
0.2
0.4
0.6
0.8
1.0
1.2
1.4
1.6
1.8
2.0
I_u
$\omega d/V_s$
E_p/E_s=10000
E_p/E_s=1000
E_p/E_s=500
E_p/E_s=200
E_p/E_s=100

Figure 11

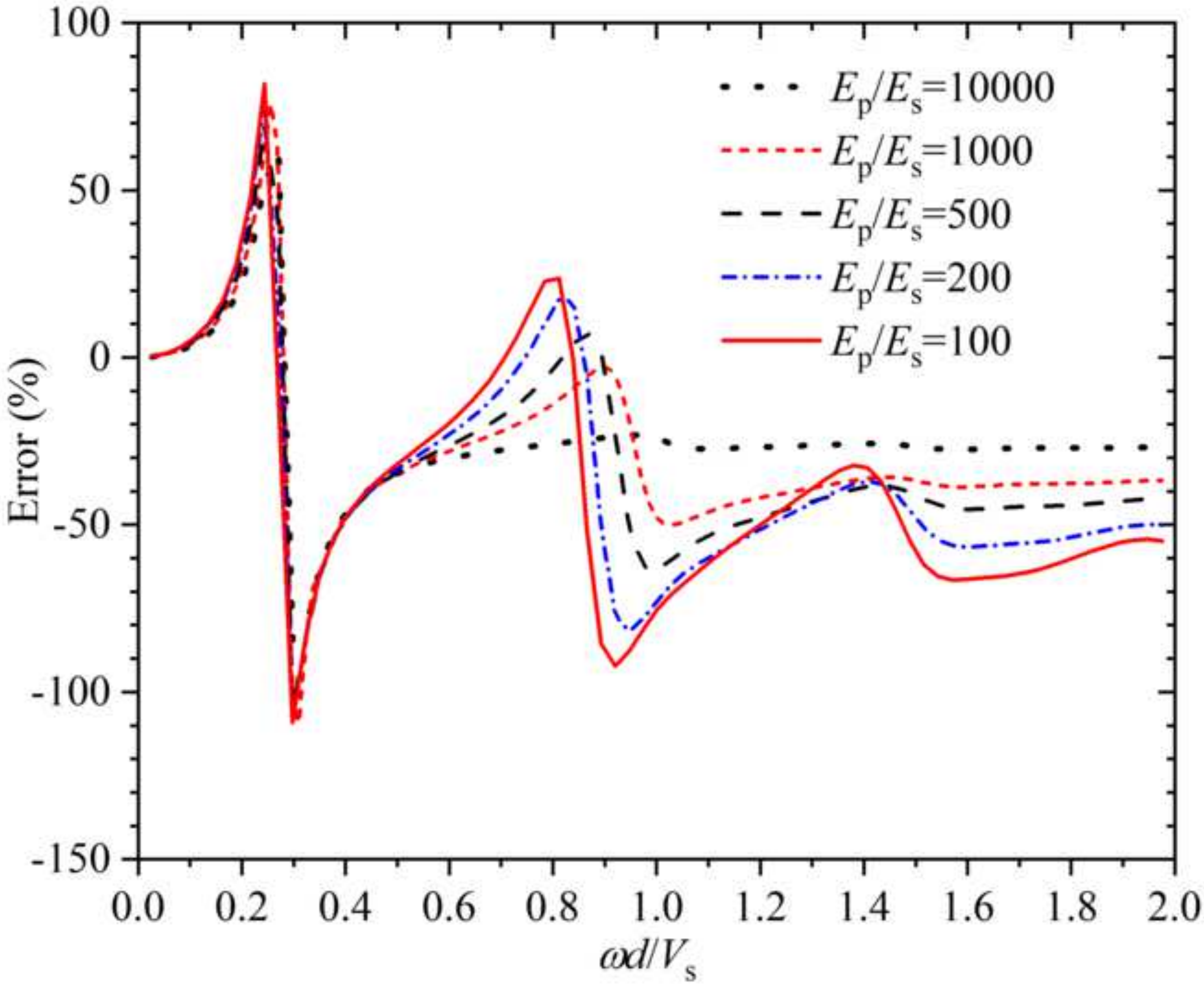

100
50
0
-50
-100
-150
Error (%)
0.0
0.2
0.4
0.6
0.8
1.0
1.2
1.4
1.6
1.8
2.0
$\omega d/V_s$
E_p/E_s=10000
E_p/E_s=1000
E_p/E_s=500
E_p/E_s=200
E_p/E_s=100

Figure 12

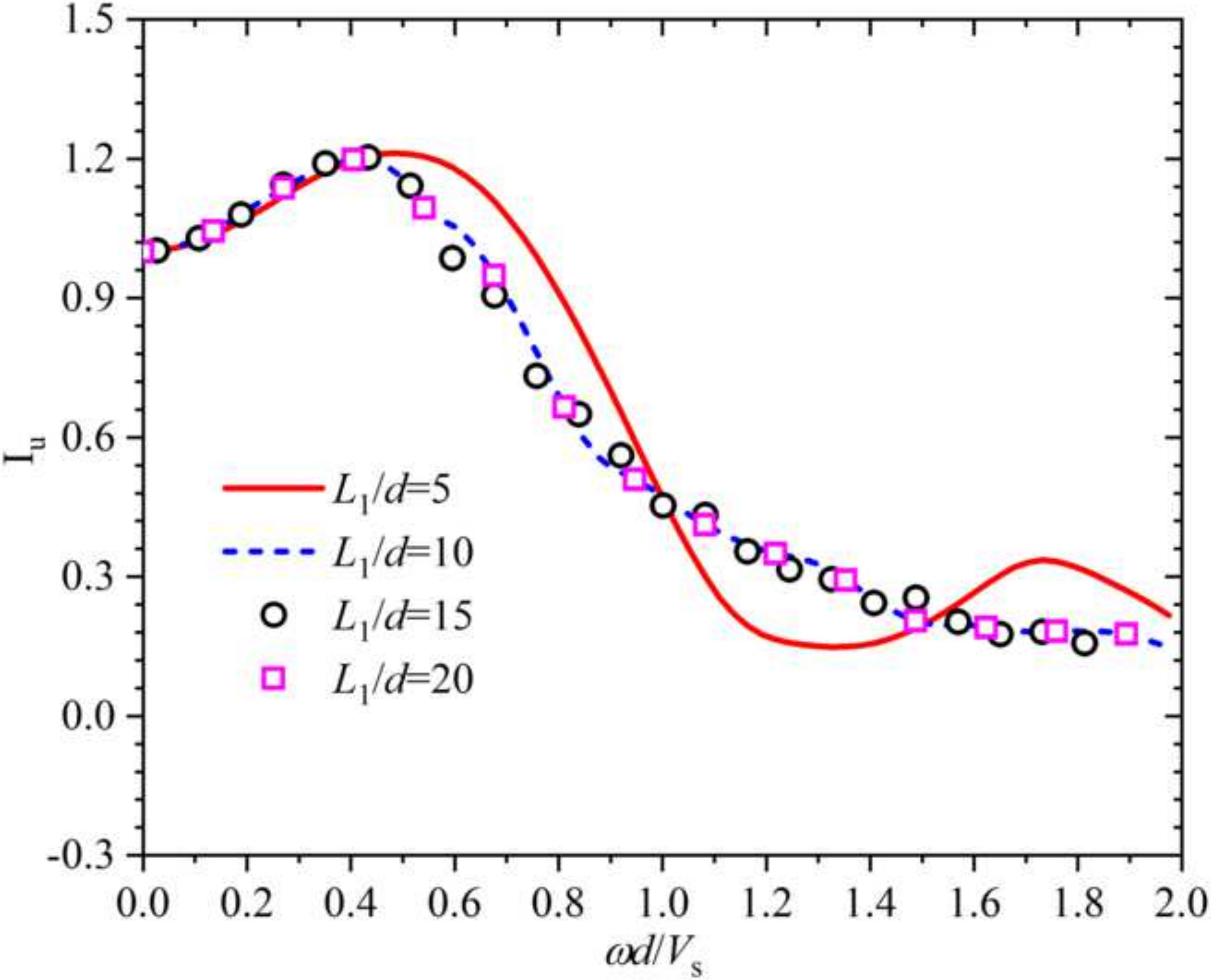

1.5
1.2
0.9
0.6
0.3
0.0
-0.3
I_u
L_1/d=5
L_1/d=10
L_1/d=15
L_1/d=20
0.0
0.2
0.4
0.6
0.8
1.0
1.2
1.4
1.6
1.8
2.0
$\omega d/V_s$

Figure13

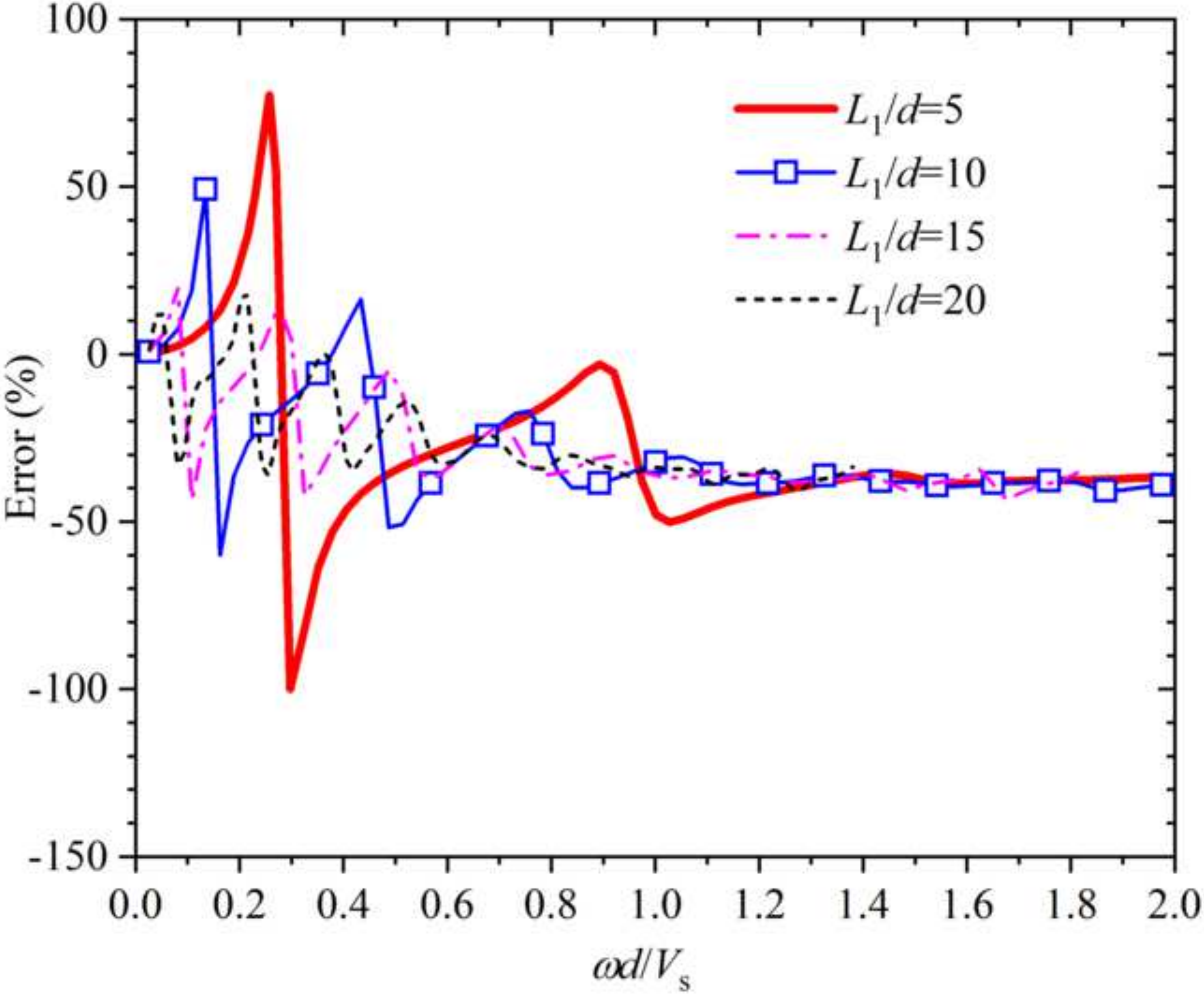

100
50
0
-50
-100
-150
Error (%)
0.0
0.2
0.4
0.6
0.8
1.0
1.2
1.4
1.6
1.8
2.0
$\omega d/V_s$
L_1/d=5
L_1/d=10
L_1/d=15
L_1/d=20

Figure 14a

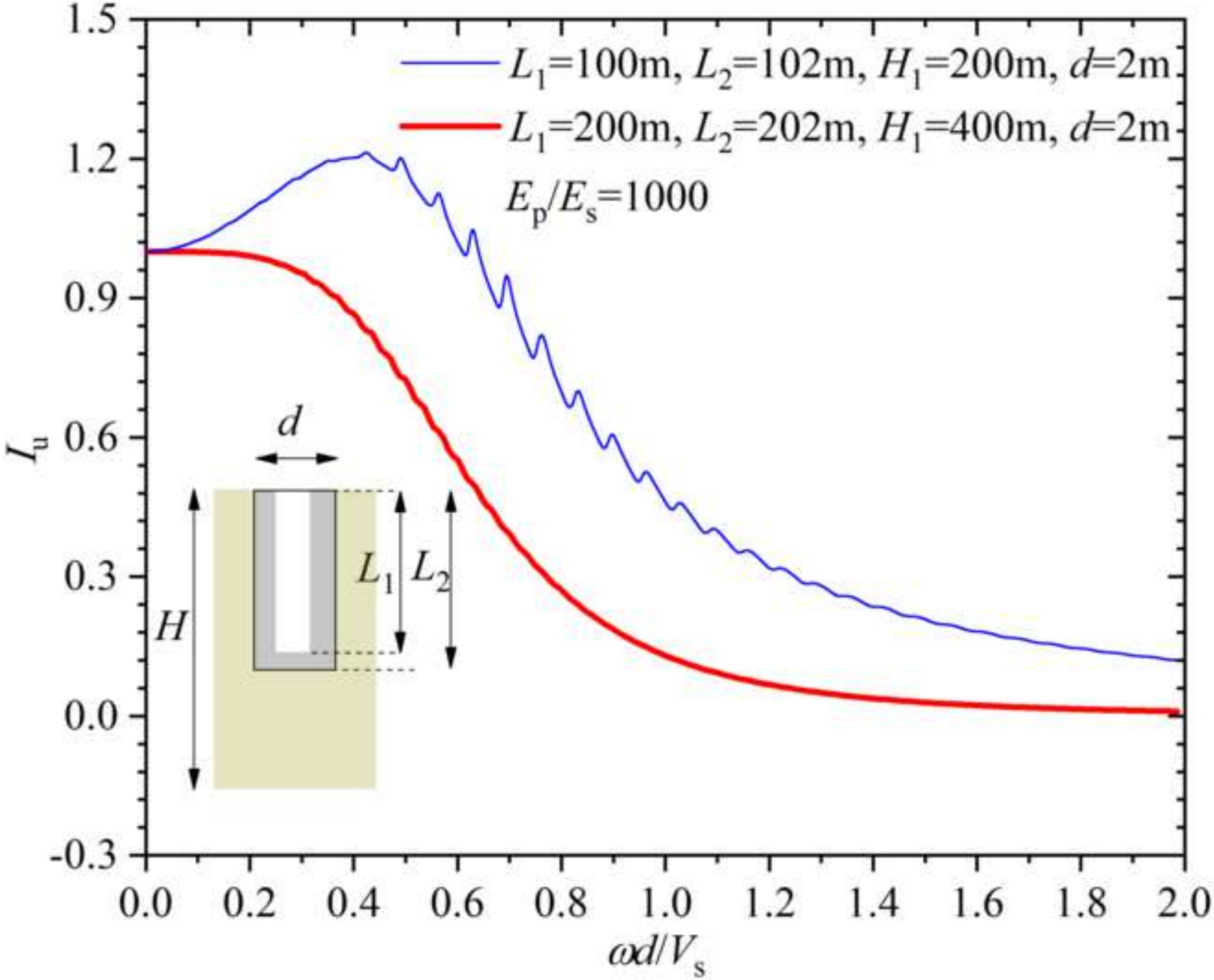

L_1=100m, L_2=102m, H_1=200m, d=2m
L_1=200m, L_2=202m, H_1=400m, d=2m
E_p/E_s=1000
I_u
$\omega d/V_s$
d
H
L_1
L_2
1.5
1.2
0.9
0.6
0.3
0.0
-0.3
0.0
0.2
0.4
0.6
0.8
1.0
1.2
1.4
1.6
1.8
2.0

Figure 14b

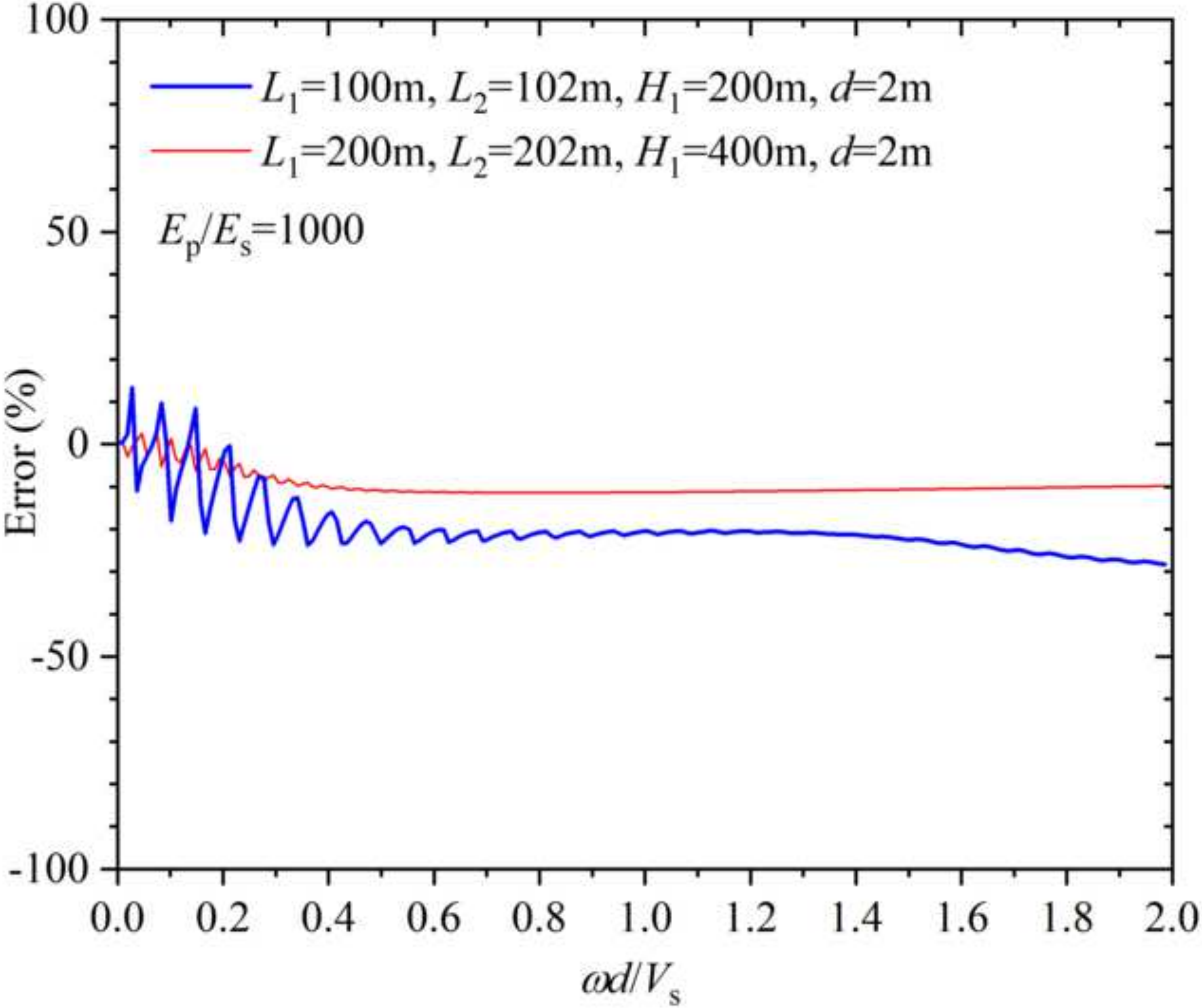

L_1=100m, L_2=102m, H_1=200m, d=2m
L_1=200m, L_2=202m, H_1=400m, d=2m
E_p/E_s=1000
Error (%)
100
50
0
-50
-100
0.0
0.2
0.4
0.6
0.8
1.0
1.2
1.4
1.6
1.8
2.0
$\omega d/V_s$

Figure 15a

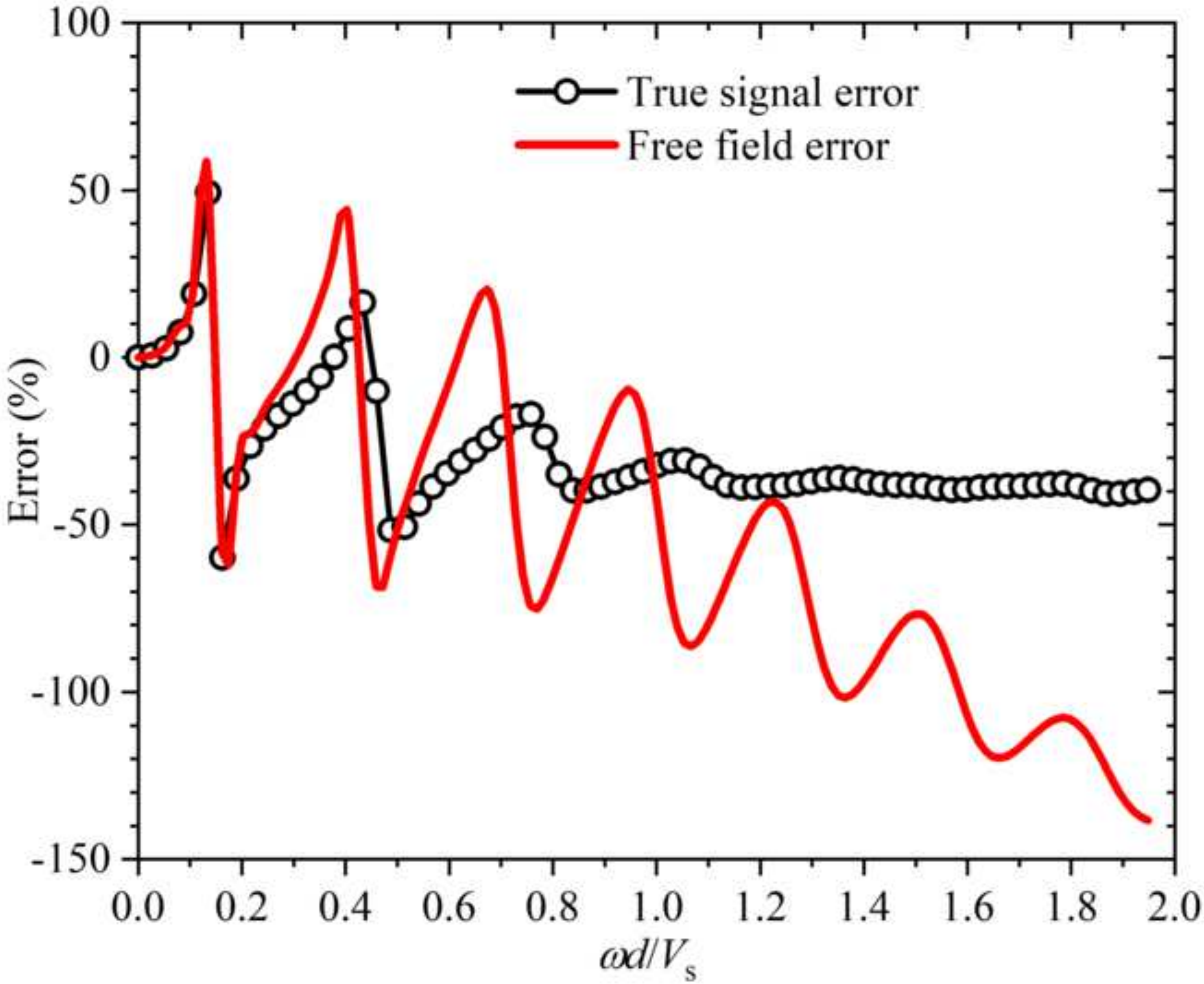

True signal error
Free field error
100
50
0
-50
-100
-150
Error (%)
0.0
0.2
0.4
0.6
0.8
1.0
1.2
1.4
1.6
1.8
2.0
$\omega d/V_s$

Figure 15b

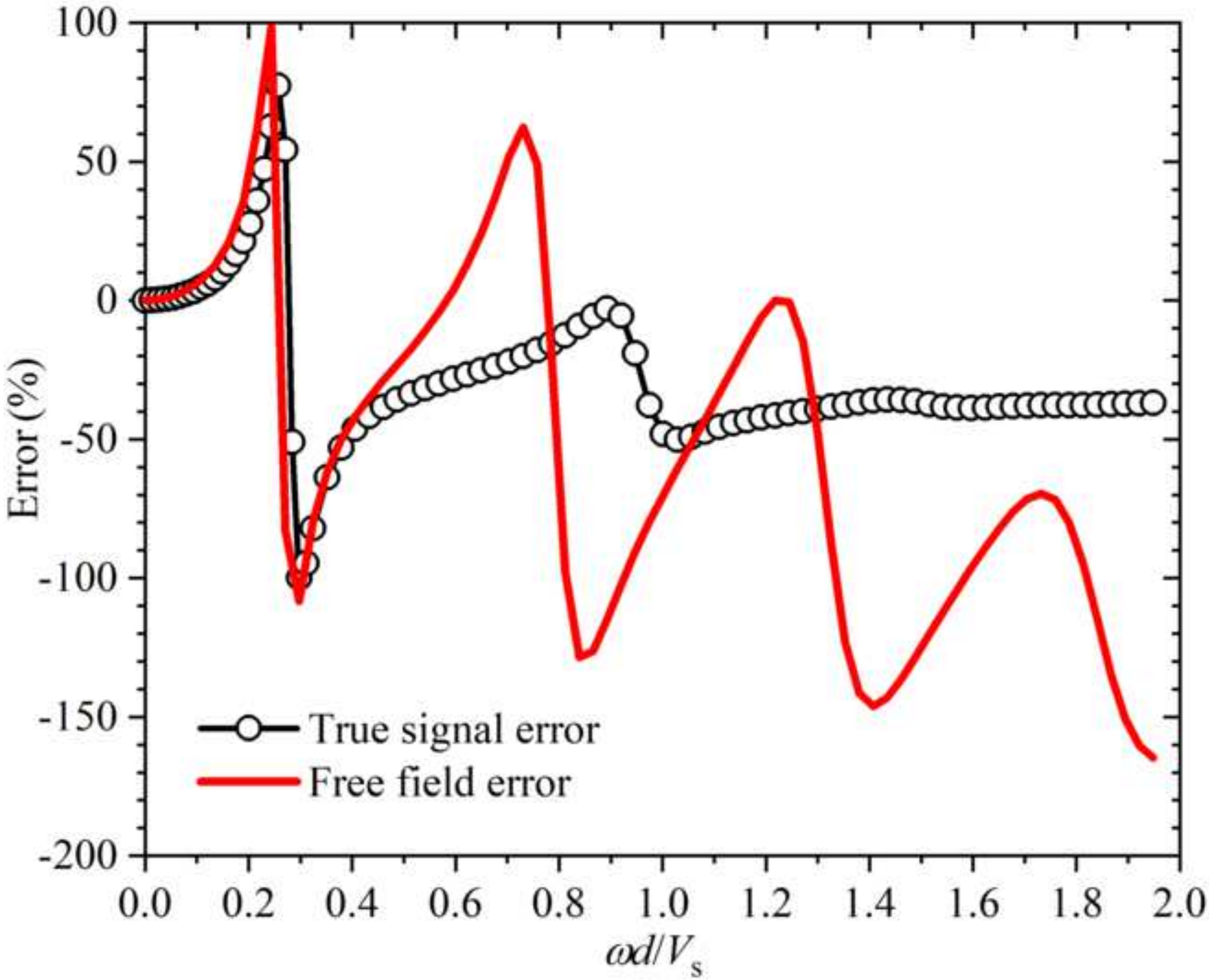

100
50
0
-50
-100
-150
-200
Error (%)
0.0
0.2
0.4
0.6
0.8
1.0
1.2
1.4
1.6
1.8
2.0
$\omega d/V_s$
True signal error
Free field error

Figure 15c

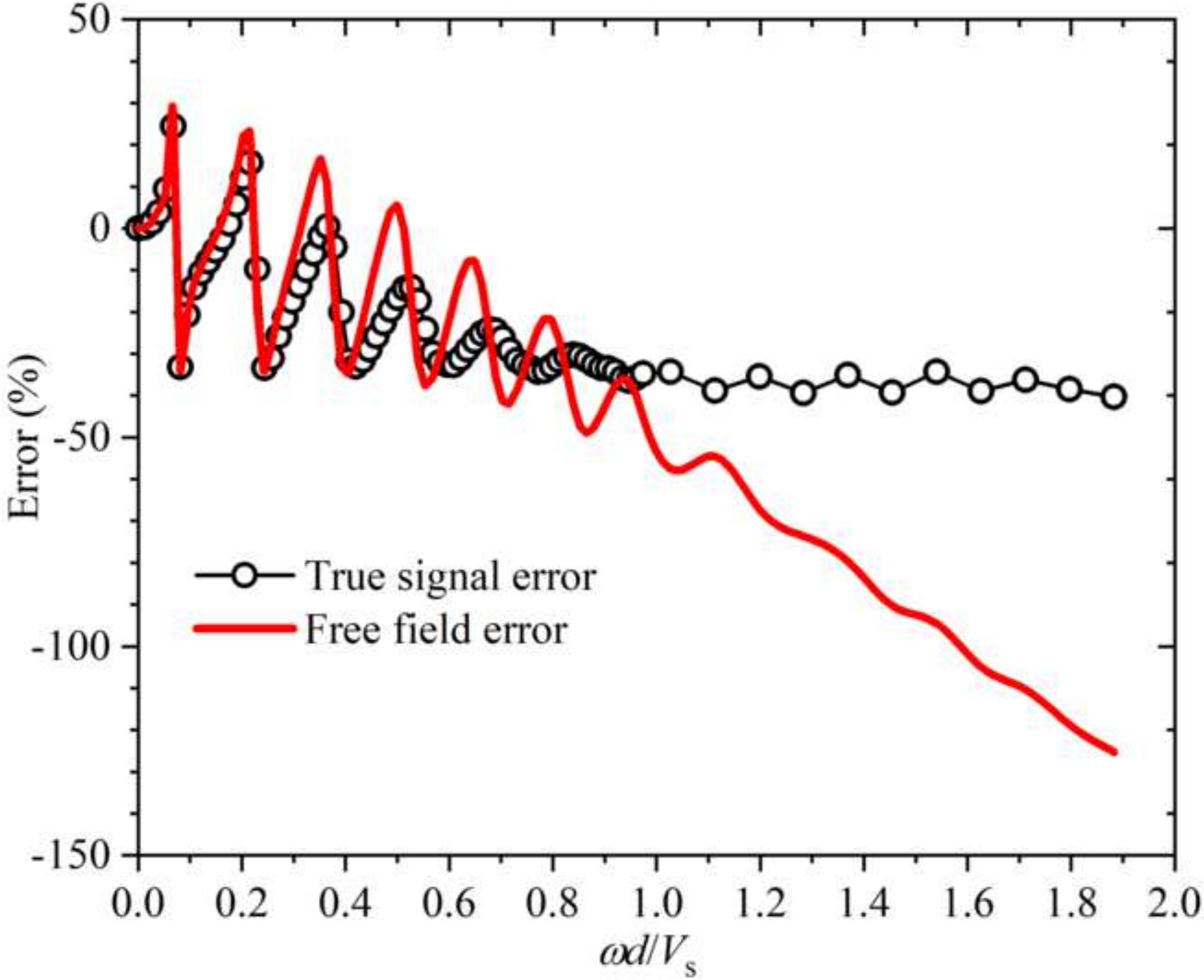

50
0
-50
-100
-150
0.0
0.2
0.4
0.6
0.8
1.0
1.2
1.4
1.6
1.8
2.0
Error (%)
$\omega d/V_s$
True signal error
Free field error

Figure 16a

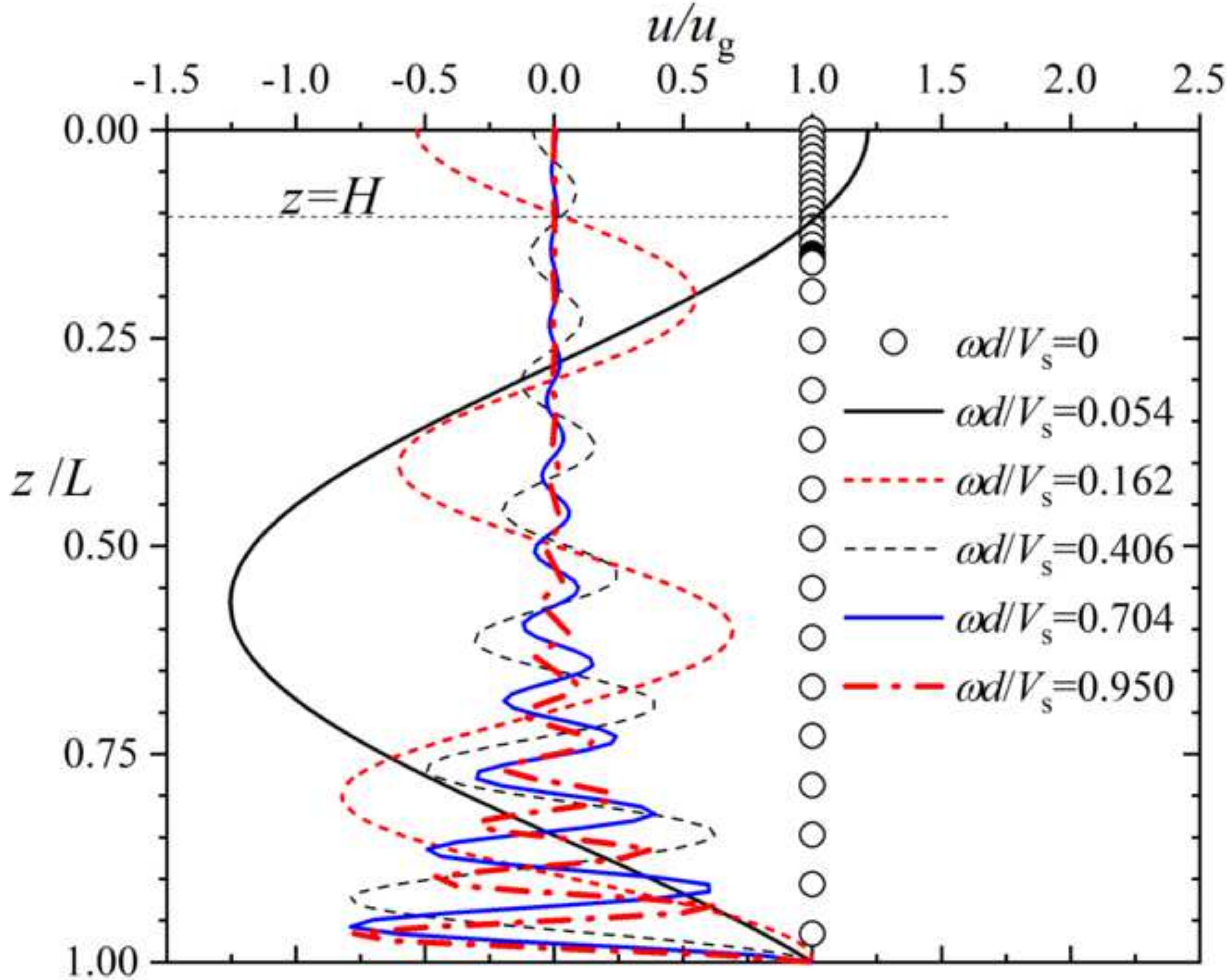

u/u_g
-1.5 -1.0 -0.5 0.0 0.5 1.0 1.5 2.0 2.5
0.00
0.25
0.50
0.75
1.00
z/L
$z=H$
$\omega d/V_s=0$
$\omega d/V_s=0.054$
$\omega d/V_s=0.162$
$\omega d/V_s=0.406$
$\omega d/V_s=0.704$
$\omega d/V_s=0.950$

Figure 16b

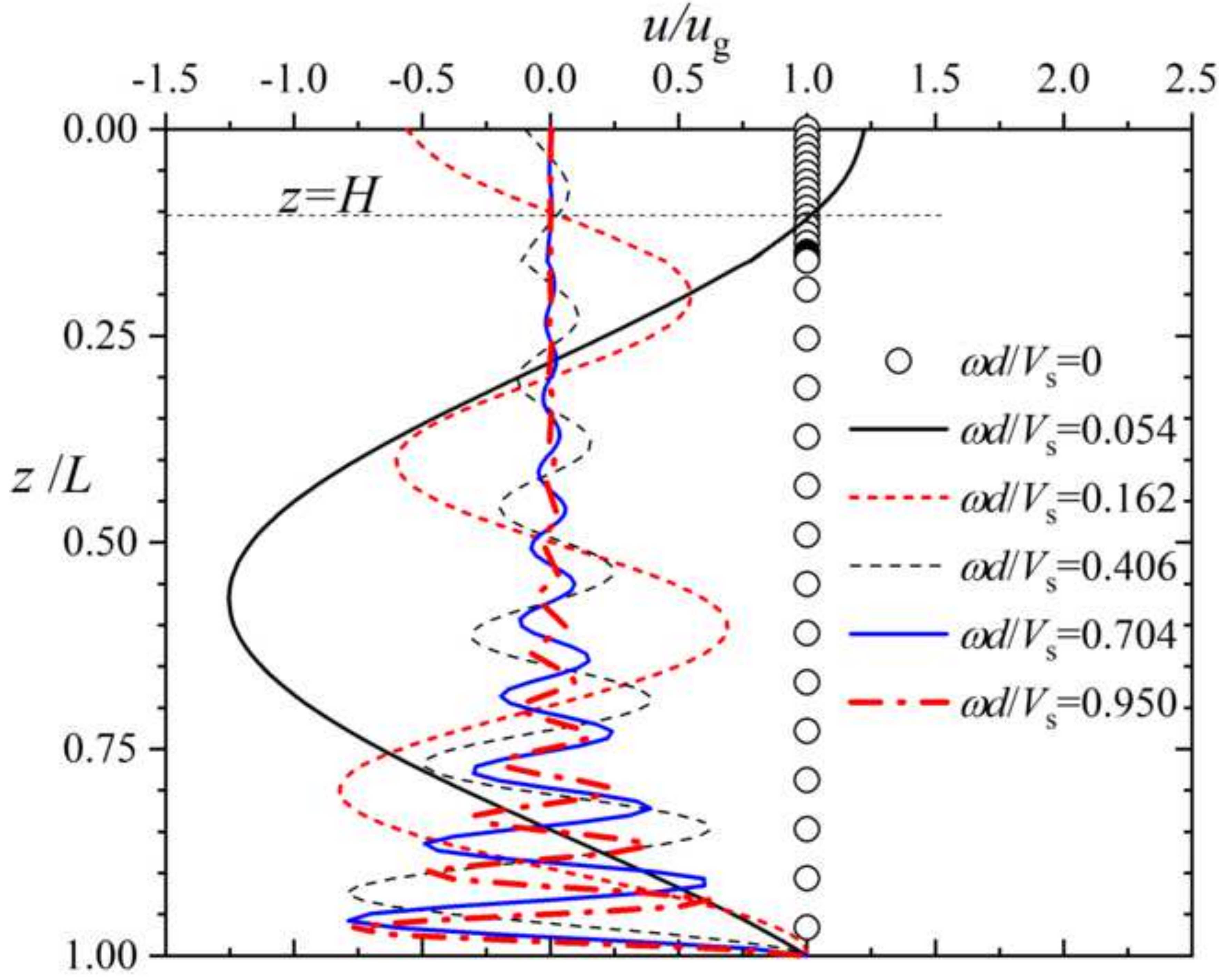

u/u_g
-1.5
-1.0
-0.5
0.0
0.5
1.0
1.5
2.0
2.5
0.00
0.25
0.50
0.75
1.00
z/L
$z=H$
$\omega d/V_s=0$
$\omega d/V_s=0.054$
$\omega d/V_s=0.162$
$\omega d/V_s=0.406$
$\omega d/V_s=0.704$
$\omega d/V_s=0.950$

Figure 16c

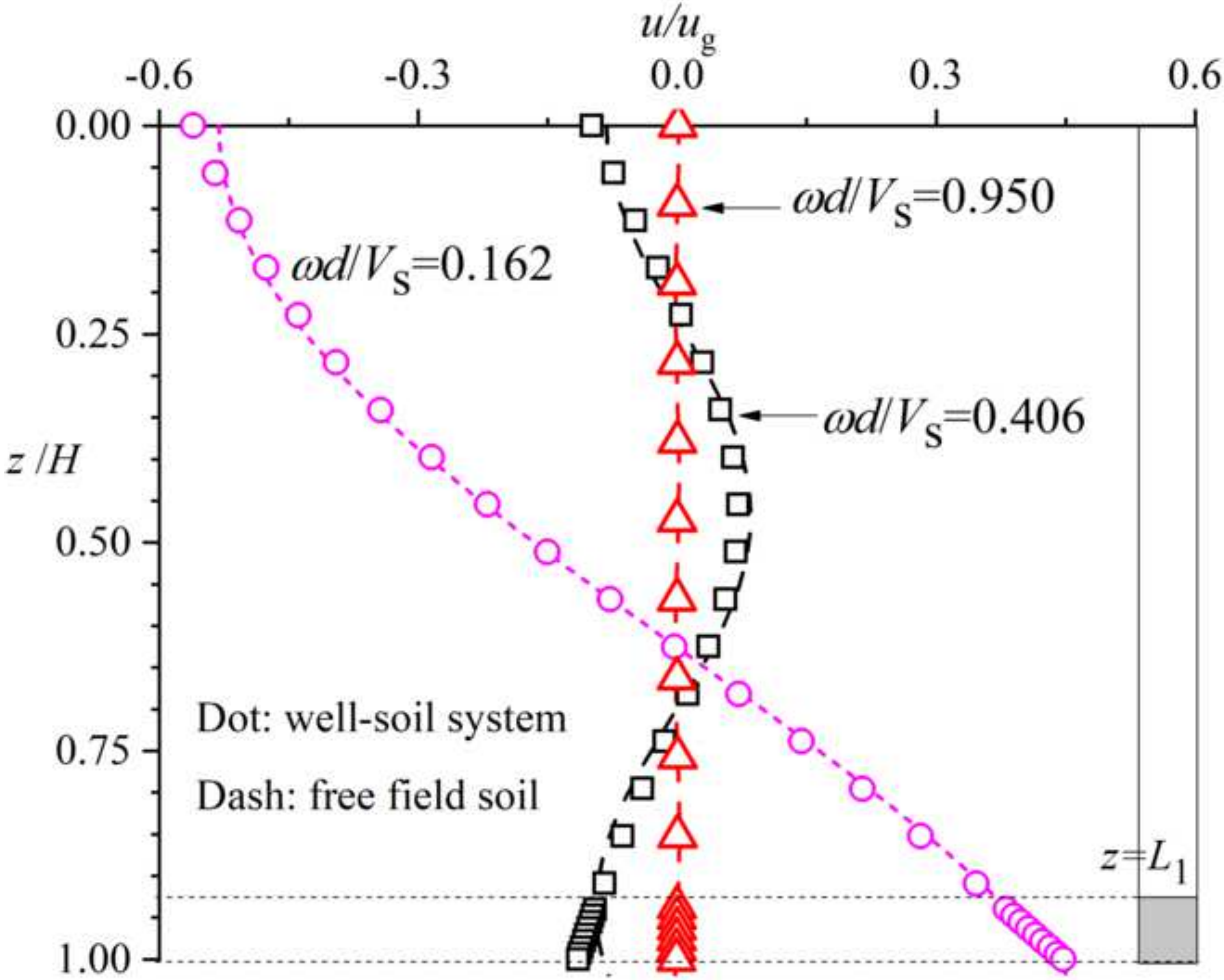

u/u_g
-0.6
-0.3
0.0
0.3
0.6
0.00
0.25
0.50
0.75
1.00
z/H
$\omega d/V_S$=0.950
$\omega d/V_S$=0.162
$\omega d/V_S$=0.406
Dot: well-soil system
Dash: free field soil
$z=L_1$

Figure 17a

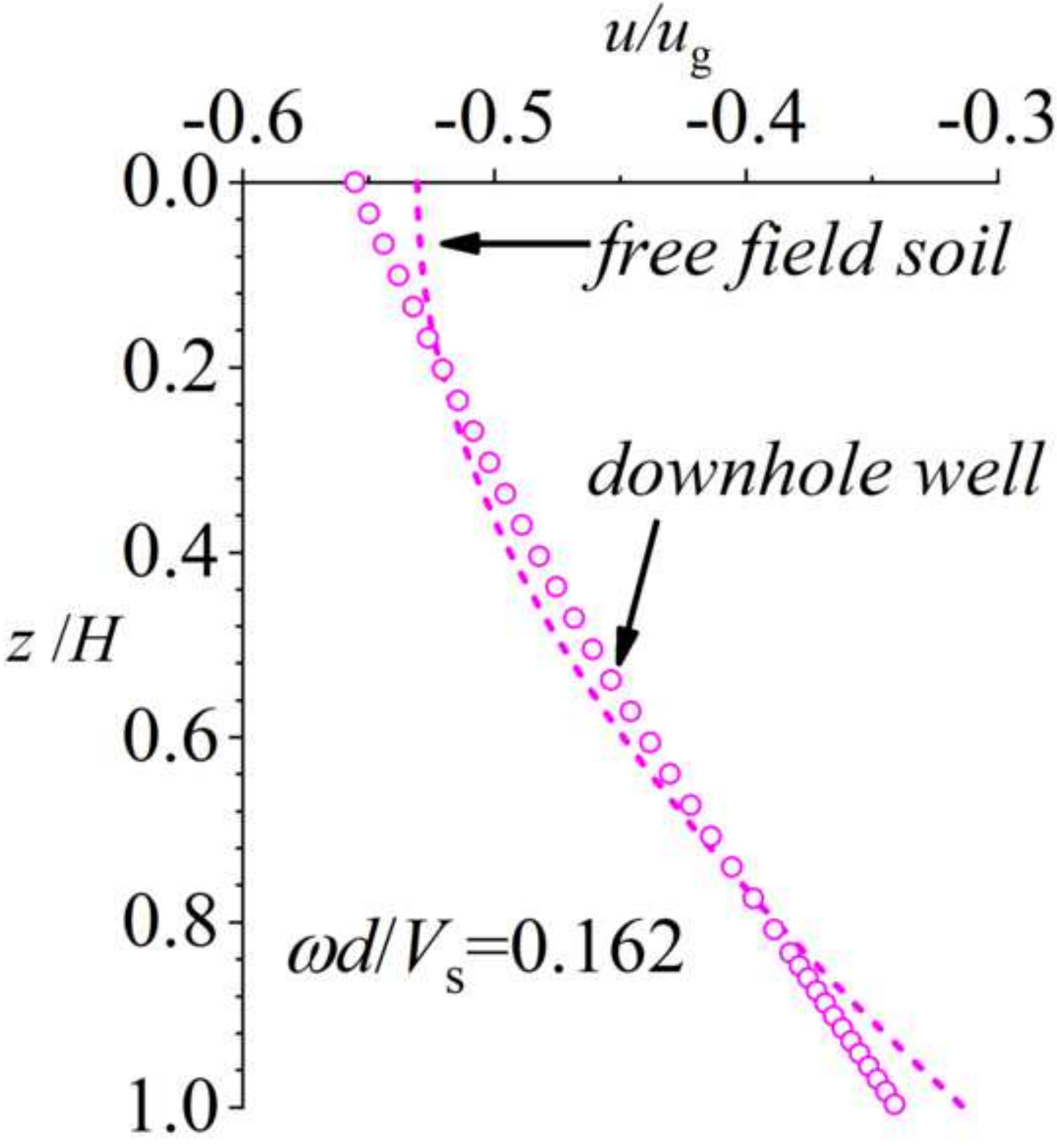

u/u_g
-0.6
-0.5
-0.4
-0.3
0.0
0.2
0.4
0.6
0.8
1.0
z/H
free field soil
downhole well
$\omega d/V_s$=0.162

Figure 17b

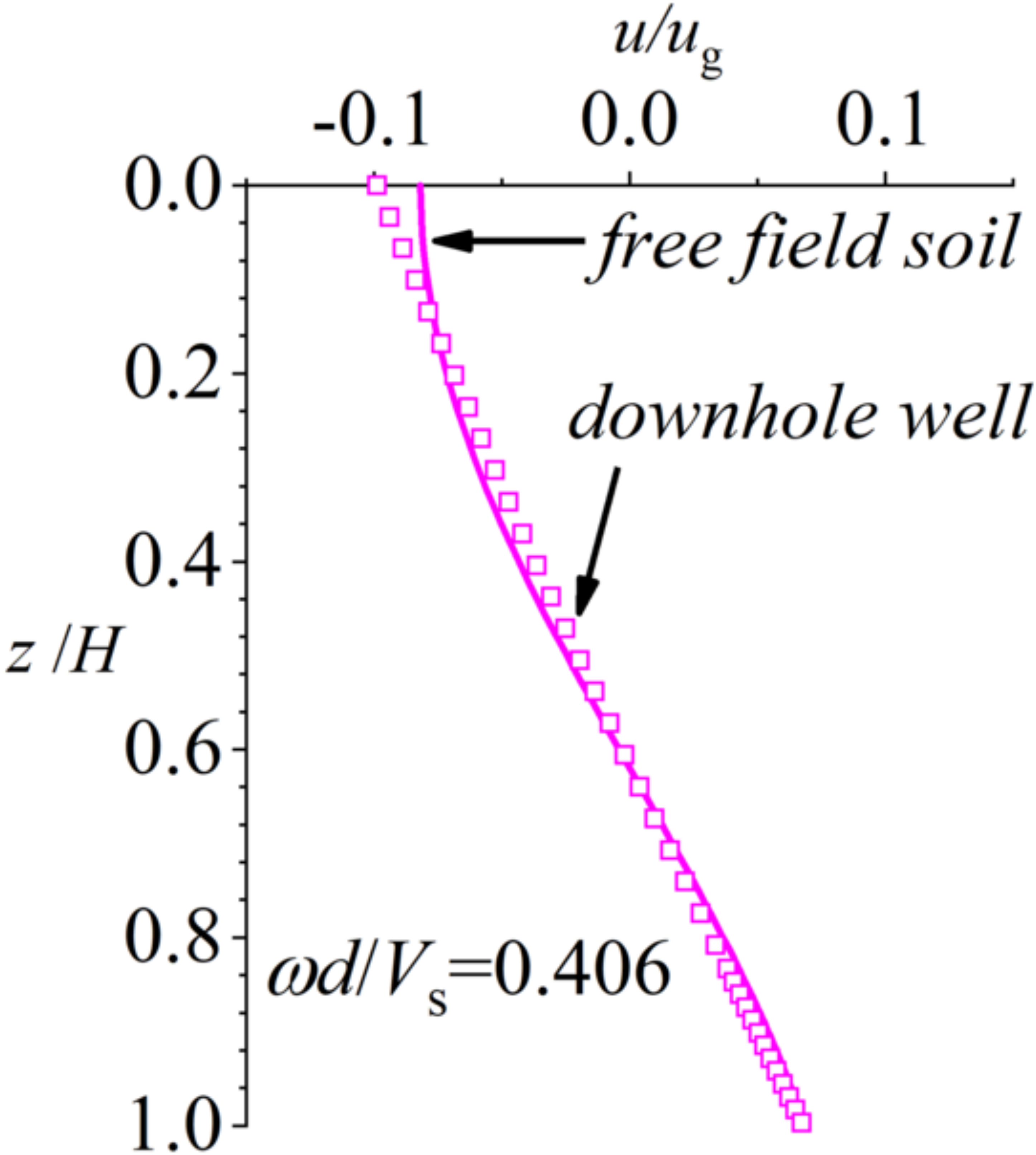

u/u_g
-0.1
0.0
0.1
0.0
0.2
0.4
0.6
0.8
1.0
z/H
free field soil
downhole well
$\omega d/V_s$=0.406

Figure 17c

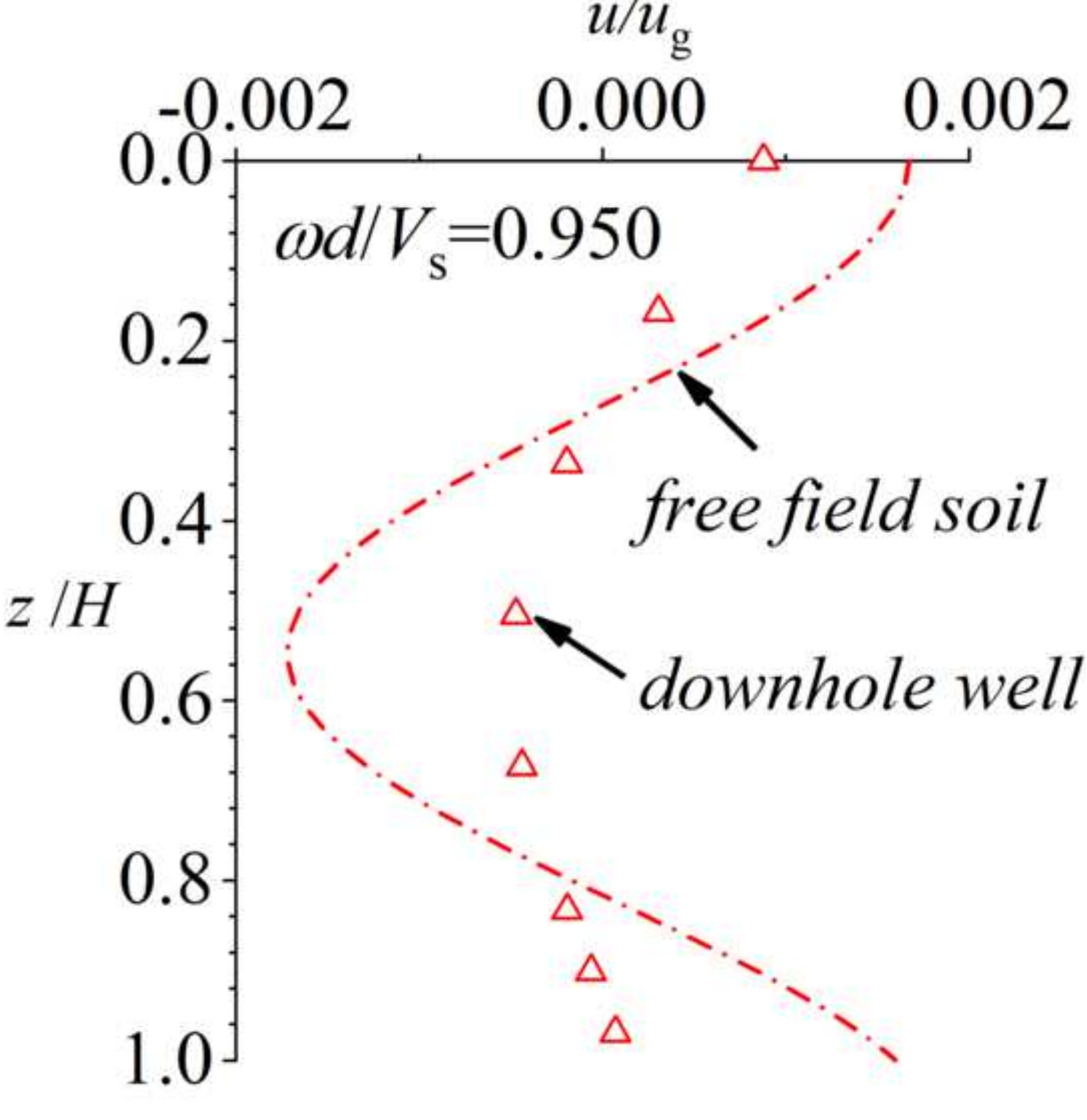

u/u_g
-0.002
0.000
0.002
0.0
$\omega d/V_s$=0.950
0.2
0.4
free field soil
z/H
downhole well
0.6
0.8
1.0

Figure 18a

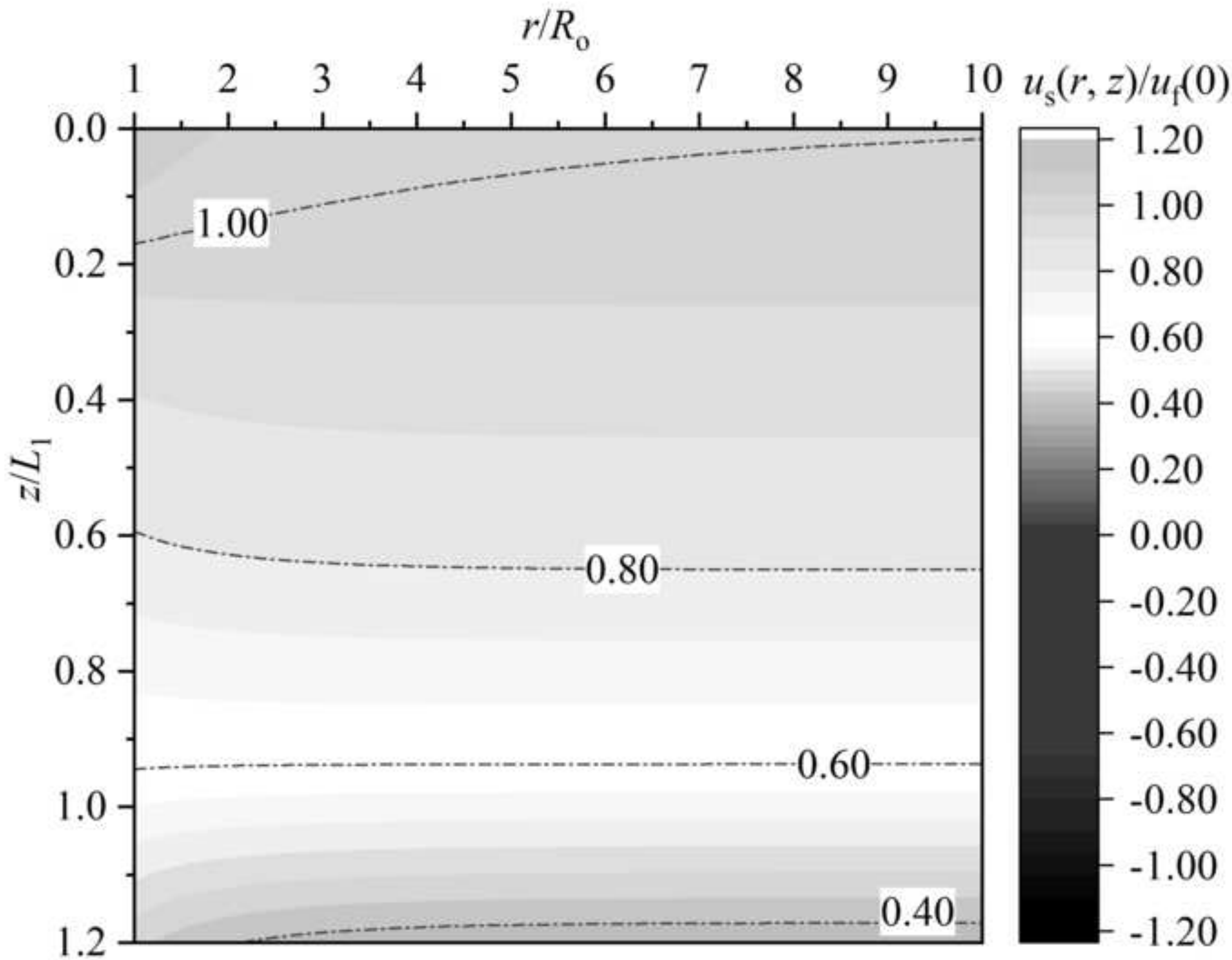

r/Ro
1
2
3
4
5
6
7
8
9
10
us(r, z)/uf(0)
0.0
0.2
0.4
0.6
0.8
1.0
1.2
z/L1
1.00
0.80
0.60
0.40
1.20
1.00
0.80
0.60
0.40
0.20
0.00
-0.20
-0.40
-0.60
-0.80
-1.00
-1.20

Figure 18b

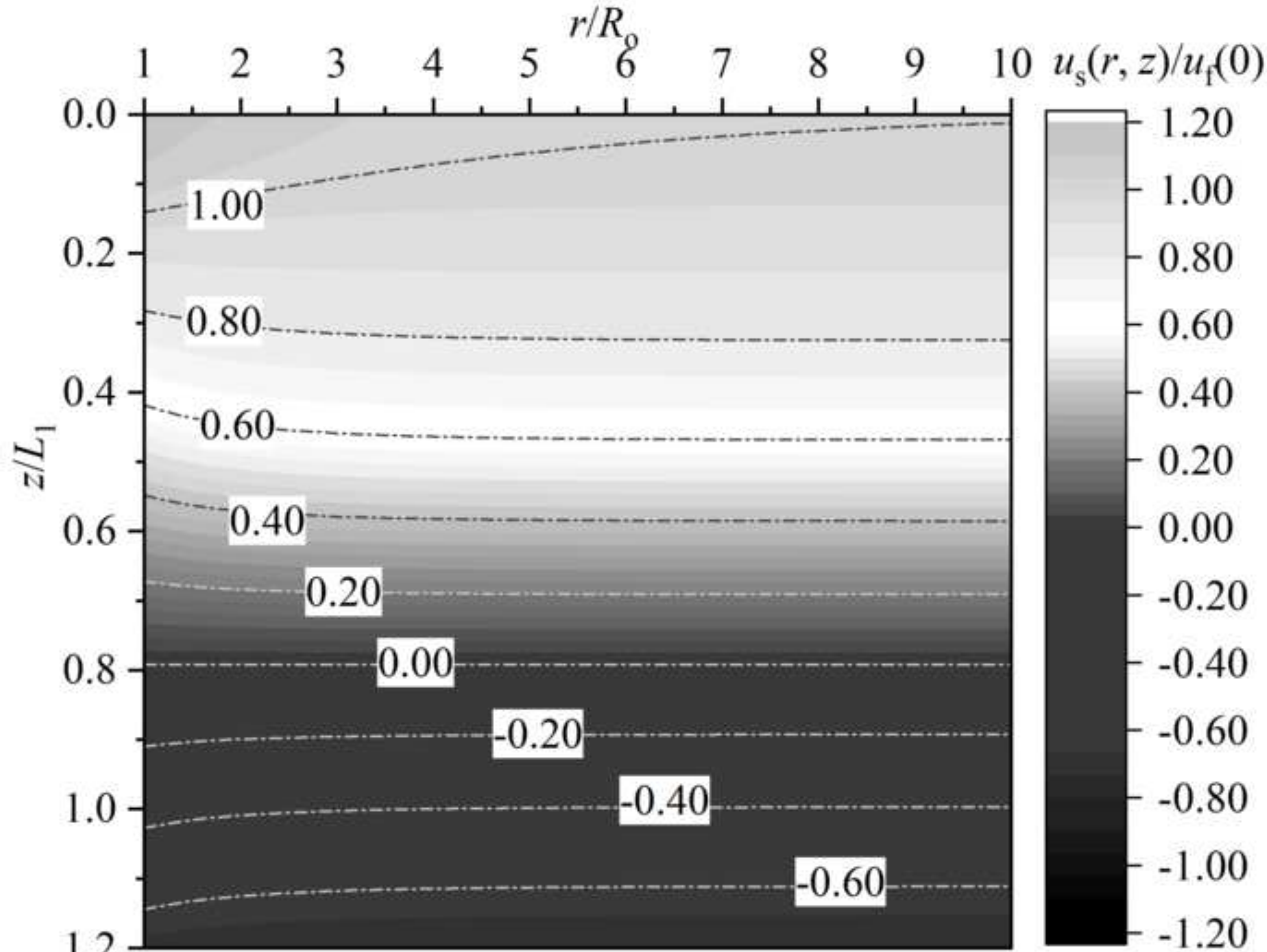

r/R_o
1
2
3
4
5
6
7
8
9
10
$u_s(r, z)/u_f(0)$
0.0
0.2
0.4
0.6
0.8
1.0
1.2
z/L_1
1.00
0.80
0.60
0.40
0.20
0.00
-0.20
-0.40
-0.60
1.20
1.00
0.80
0.60
0.40
0.20
0.00
-0.20
-0.40
-0.60
-0.80
-1.00
-1.20

Figure 18c

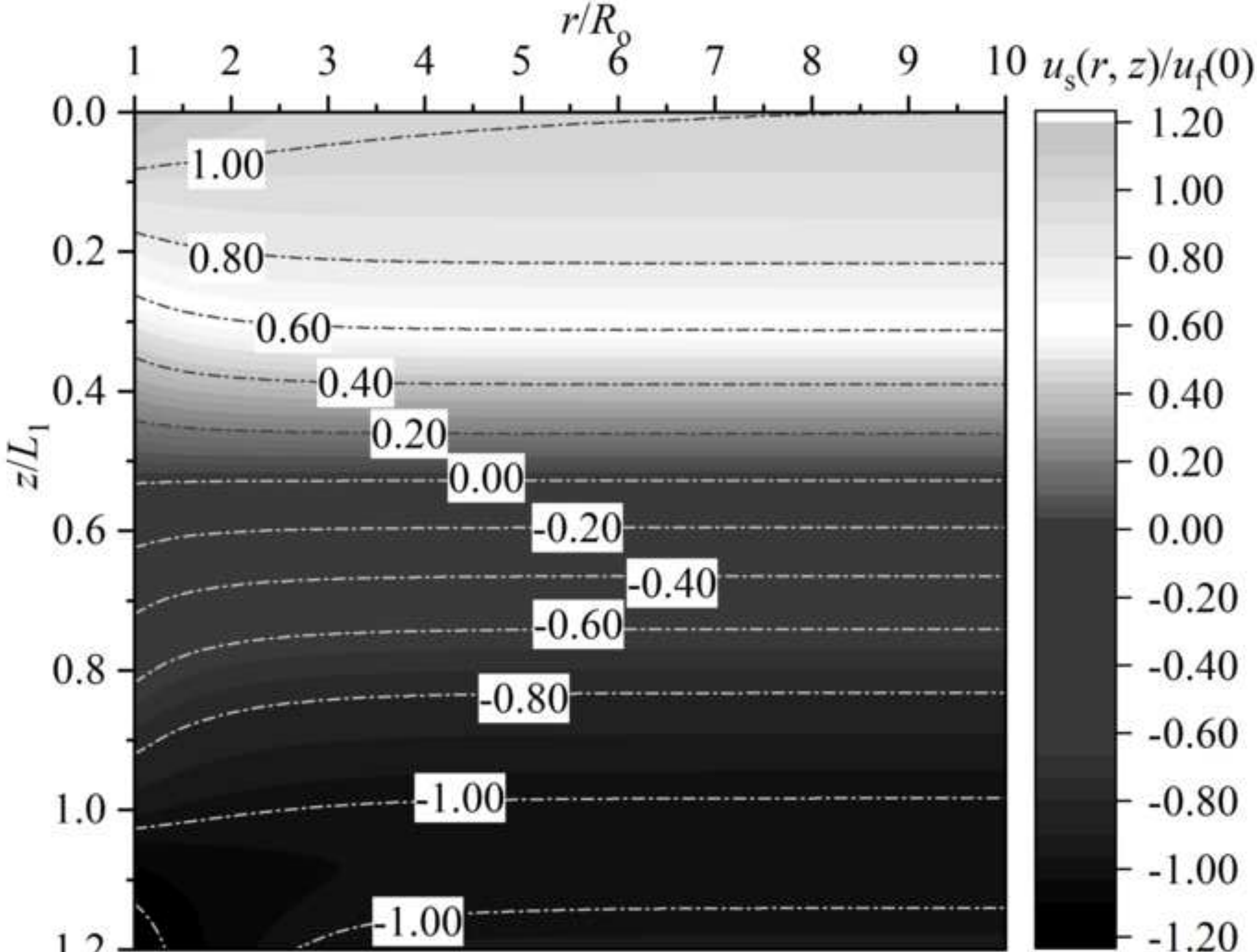
r/R_0
1
2
3
4
5
6
7
8
9
10
$u_s(r, z)/u_f(0)$
0.0
0.2
0.4
0.6
0.8
1.0
1.2
z/L_1
1.00
0.80
0.60
0.40
0.20
0.00
-0.20
-0.40
-0.60
-0.80
-1.00
-1.00
1.20
1.00
0.80
0.60
0.40
0.20
0.00
-0.20
-0.40
-0.60
-0.80
-1.00
-1.20

Figure 18d

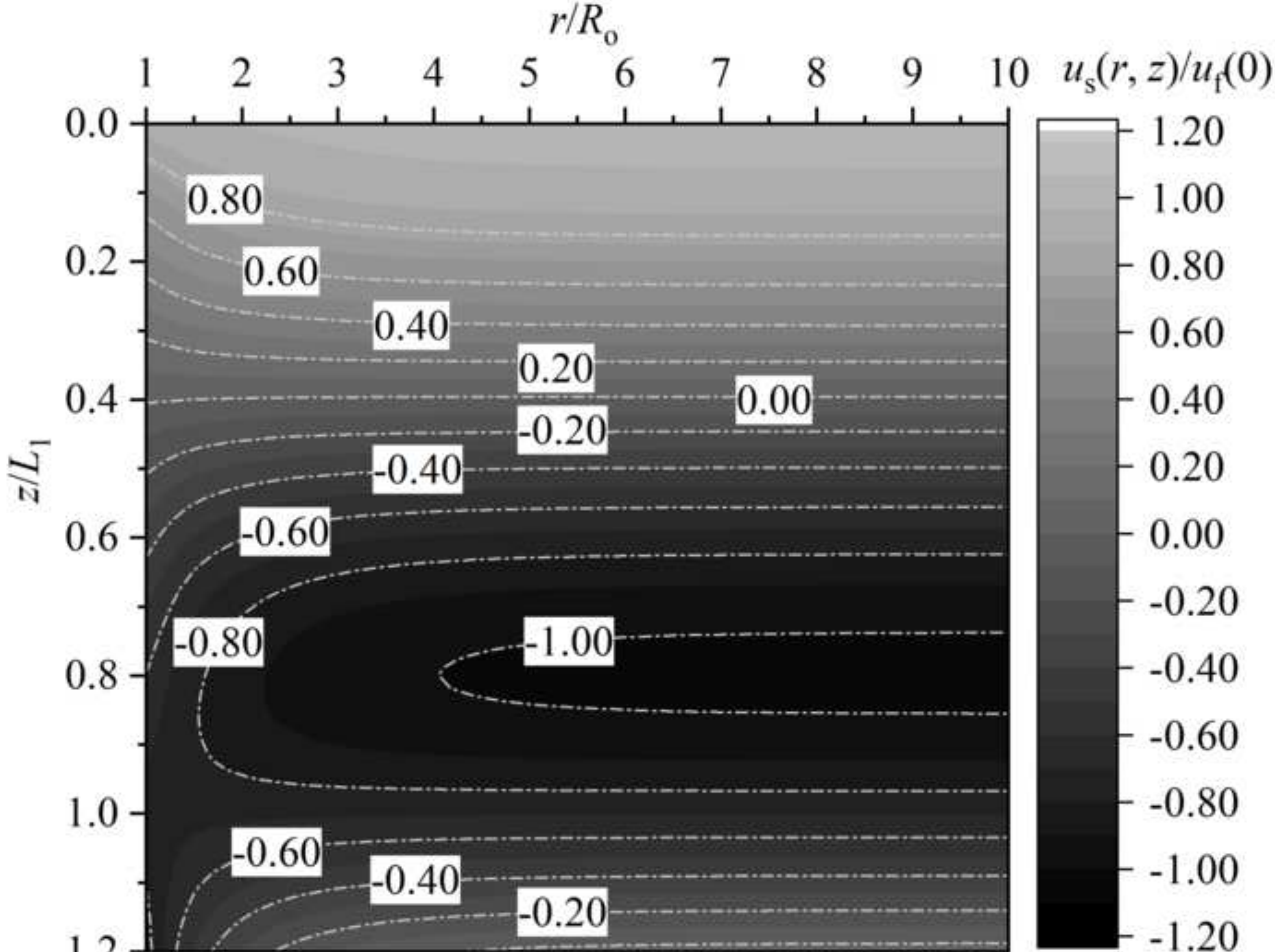

r/R_o
1
2
3
4
5
6
7
8
9
10
$u_s(r, z)/u_f(0)$
z/L_1
0.0
0.2
0.4
0.6
0.8
1.0
1.2
0.80
0.60
0.40
0.20
0.00
-0.20
-0.40
-0.60
-0.80
-1.00
-0.60
-0.40
-0.20
1.20
1.00
0.80
0.60
0.40
0.20
0.00
-0.20
-0.40
-0.60
-0.80
-1.00
-1.20

Figure caption list

Fig. 1 Train derailment and viaduct damage on earthquake

Fig. 2 Difference between P-wave and S-wave in earthquake monitoring system

Fig. 3 Downhole well subjected to vertically incident S-waves: soil–well system and definition of coordinate system.

Fig. 4 Flow chart of the iterative algorithm in this study

Fig. 5 Converge process of q with the iteration cycles for the seismic response of a downhole well. E_p/E_s=1000; ρ_s/ρ_p=0.7; R_i/R_o=0.9; L_1/d=9.5; H/d=10.0; L=22.5d. (a)Real part of q; (b)Imaginary part of q

Fig. 6 Comparisons of kinematic response factor I_u of a solid pile from this present solution with those from existing methods. ρ_s/ρ_p=0.7; R_i=0; L=20d=40R_o.

Fig. 7. Geometry and Meshes of the numerical simulation for seismic response of well-soil system.

Fig. 8 Seismic displacement histories of well-soil system at various positions subjected to Gabor wavelet at a central frequency of 15Hz.

Fig. 9 Comparisons of kinematic response factor I_u of a seismic well from this present solution with numerical results. ρ_s/ρ_p=0.7; R_i=0.9m; d=2R_o=2.0m; L_1=19m; H=20m; L=45m.

Fig. 10 Variation of kinematic response factor (I_u) against non-dimensional frequency with various modulus ratios. ρ_s/ρ_p=0.7; R_i/R_o=0.9; L_1/d=5; H/d=6; L=40d.

Fig. 11 Variation of monitoring error against non-dimensional frequency with various modulus ratios. ρ_s/ρ_p=0.7; R_i/R_o=0.9; L_1/d=5; H/d=6; L=40d.

Fig. 12 Variation of kinematic response factor (I_u) against non-dimensional frequency with various embedded depths. ρ_s/ρ_p=0.7; R_i/R_o=0.9; (H-L_1)=d; L=100d; E_p/E_s=1000.

Fig. 13 Variation of monitoring error against non-dimensional frequency with various embedded depths. ρ_s/ρ_p=0.7; R_i/R_o=0.9; (H-L_1) =d; L=100d; E_p/E_s=1000.

Fig. 14 Variations of kinematic response factor (I_u) and monitoring error against non-dimensional frequency for the deep borehole. ρ_s/ρ_p=0.7; R_i/R_o=0.9; E_p/E_s=1000. (a)Kinematic response factor (b) Monitoring error

Fig. 15 Frequency-dependent relative displacement error. ρ_s/ρ_p=0.7; R_i/R_o=0.9; (H-L_1) =d;

E_p/E_s=1000; L=100d. (a) L_1=5d ;(b) L_1=10d ; (c) L_1=20d

Fig. 16 Comparisons of displacement profiles along depth for well-soil system and free field soil when L_1=15d. ρ_s/ρ_p=0.7; R_i/R_o=0.9; H-L_1=d; E_p/E_s=1000; L=100d. (a) Displacement profiles within $z<L$ for free field soil (b)Displacement profiles within $z<L$ for well-soil system (c) Comparison of displacement profiles within $z<H$ between well-soil system and free field soil

Fig. 17 Comparisons of displacement variations along well depth for well-soil system and free field soil when L_1=5d. ρ_s/ρ_p=0.7; R_i/R_o=0.9; (H-L_1) =d; E_p/E_s=1000; L=100d.

Fig. 18 Influences of frequency on the contours of the normalized transverse displacement of the soil-well system with respect to the free field displacement on the ground surface. ρ_s/ρ_p=0.7; R_i/R_o=0.9; H-L_1=d; L_1=5d; E_p/E_s=1000; L=100d. (a)ωd/Vs=0.2, Er=26.1%; (b) ωd/Vs=0.4, Er=-47.6%; (c) ωd/Vs=0.6, Er=-28.0%; (d) ωd/Vs=0.8, Er=-13.9%